

THE UNIVERSITY OF CHICAGO

DATA REDUCTION AND ANALYSIS OF THE PYTHON V COSMIC  
MICROWAVE BACKGROUND ANISOTROPY EXPERIMENT

A DISSERTATION SUBMITTED TO  
THE FACULTY OF THE DIVISION OF THE PHYSICAL SCIENCES  
IN CANDIDACY FOR THE DEGREE OF  
DOCTOR OF PHILOSOPHY  
DEPARTMENT OF ASTRONOMY AND ASTROPHYSICS

BY

KIMBERLY ANN COBLE

CHICAGO, ILLINOIS

DECEMBER 1999

Copyright © 2024 by Kimberly Ann Coble

All rights reserved

*'Helped are those who love the entire cosmos... for to them will be shown  
the unbroken web of life and the meaning of infinity.'*

Alice Walker, *The Temple of My Familiar*

## ACKNOWLEDGMENTS

‘The spoken word is a jacket too tight.’

Poi Dog Pondering, *Collarbone*

I cannot adequately express in words my gratitude to the people who have helped me along my path.

I thank my advisor, Scott Dodelson, for being a good teacher, able to explain in a simple way difficult concepts, and for advice at crucial moments. I am indebted to the other members of the Python collaboration, especially Lloyd Knox for explaining sophisticated analysis techniques, John Kovac for explaining the experiment, and Ken Ganga, who did much of the work on the Python V foregrounds. I thank the MSAM collaboration, especially Steve Meyer, Jason Puchalla, Grant Wilson, Dave Cottingham, and Ed Cheng. Much of my work on window functions was done in the context of working with their group. I thank Dave Cottingham and Grant Wilson for many conversations, cross-checks and useful memos on window functions. I also thank Bharat Ratra for helpful discussions on window functions.

The many other people working on the CMB at Chicago have sparked interesting discussions and I have learned much from them. John Carlstrom taught a fantastic course on experimental techniques. The graduate stu-

dents here have been unendingly supportive, sharing scientific knowledge and always being there for each other. Aparna Venkatesan and Brad Holden especially have comiserated and celebrated with me throughout the years. I don't know how any of us would make it without Sandy "Mom" Heinz.

My family has been a continual source of love and support. Thanks Mom, Dad, and Kellie.

To Sarah Lord, your cleverness and caring inspire me. To Chris Newell, thank you for feeding my body and soul. Your love of life and thoughtfulness are contagious. To Erik Leitch, thank you for countless conversations on the CMB, on making the transition from graduate student to graduate, and on life. You make the best pizza in Chicago.

And finally, I thank Mark Dragovan, without whom this thesis would not be possible. Thank you for giving me the opportunity to work on Python, for your encouragement, and for being a Mentor.

# TABLE OF CONTENTS

ACKNOWLEDGMENTS . . . . .	iv
LIST OF FIGURES . . . . .	viii
LIST OF TABLES . . . . .	x
ABSTRACT . . . . .	xi
Chapter	
1. INTRODUCTION . . . . .	1
1.1 Theory . . . . .	2
1.2 Temperature Anisotropy Experiments . . . . .	4
2. THE PYTHON EXPERIMENT . . . . .	10
2.1 Introduction to the Python Experiment . . . . .	10
2.2 Instrument . . . . .	11
2.3 Calibration . . . . .	14
2.4 Observations . . . . .	17
2.4.1 Observing Regions . . . . .	18
2.4.2 Observing Strategy . . . . .	18
2.4.3 Pointing . . . . .	21
2.4.4 Beam . . . . .	23
3. DATA REDUCTION . . . . .	25
3.1 Data Cuts . . . . .	25
3.2 Modulations . . . . .	26
3.3 Instrument Transfer Function . . . . .	29
3.4 Chopper Synchronous Offset . . . . .	31
3.5 Ground Shield Offset . . . . .	35
3.6 Co-adding . . . . .	37
3.7 60 Hz . . . . .	38
4. DATA ANALYSIS TECHNIQUES . . . . .	39
4.1 Bayesian Likelihood Analysis . . . . .	39
4.2 Window Functions . . . . .	41
4.2.1 A Method For Calculating Window Functions . . . . .	41

4.2.2	Normalization of the Beam Map . . . . .	46
4.2.3	Approximations . . . . .	46
4.2.4	Analytic Expressions . . . . .	47
4.2.5	Python V Window Functions . . . . .	54
4.3	KL Decomposition . . . . .	55
4.4	Constraint Matrices For Offsets . . . . .	57
5.	SINGLE MODULATION ANALYSIS . . . . .	61
5.1	Power Spectrum Constraints . . . . .	61
5.2	Noise Model . . . . .	63
5.3	Internal Consistency Checks . . . . .	68
5.3.1	$\chi^2$ Tests . . . . .	69
5.3.2	$\beta$ Tests . . . . .	69
5.3.3	KL Decomposition . . . . .	70
6.	CROSS-MODULATION ANALYSIS . . . . .	73
6.1	Noise Model and Consistency Checks . . . . .	73
6.2	Map Making . . . . .	78
6.2.1	Power Spectrum Constraints . . . . .	81
6.2.2	CMB Images . . . . .	83
6.3	Comparisons With Other Experiments . . . . .	84
6.3.1	Power Spectrum Comparison . . . . .	84
6.3.2	Comparing PyV and PyIII Maps . . . . .	84
7.	FOREGROUNDS . . . . .	87
8.	CONCLUSIONS . . . . .	91
	REFERENCES . . . . .	94

## LIST OF FIGURES

Figure	Page
1	Model CMB angular power spectra for various cosmological parameters. . . . . 5
2	CMB anisotropy measurements as of Feb 1999. . . . . 9
3	Schematic diagram of the receiver. . . . . 12
4	Bandpasses for the 4 data channels. . . . . 13
5	Schematic diagram of the Python telescope. . . . . 14
6	Picture of the Python telescope without the ground shield. . . . 15
7	A view of the Python telescope and surrounding labs. . . . . 16
8	IRAS 100 $\mu m$ view of the galaxy with the Python observing regions superimposed. . . . . 19
9	Center positions of the Python V fields. . . . . 20
10	Motion of the chopper. . . . . 21
11	Observing sets. . . . . 22
12	Pointing of the two feeds on the sky. . . . . 22
13	The data are modulated with cosines which have been apodized by a Hann window. Three of the modulations are shown. . . . . 27
14	Timestream modulations. . . . . 28
15	Frequency dependence of the instrument transfer function. . . . 29
16	Unmodulated moon data showing effect of the transfer function on the right-left phase. . . . . 30
17	Checking the phase of right and left data on the moon. . . . . 31
18	Chopper offset vs. time. . . . . 32
19	Histogram of chopper offset. . . . . 32
20	Chopper offset difference vs. time. . . . . 33
21	Histogram of chopper offset difference. . . . . 33
22	Mean chopper offset over the data set for all channels, right and left-going data vs. modulation. . . . . 34
23	Mean chopper offset difference over the data set for all channels, right and left-going data vs. modulation. . . . . 35
24	Azimuthally binned data. The signal caused by the ground shield is evident. . . . . 36
25	Amplitude of the ground shield offset as a function of declination and modulation. . . . . 37
26	Theory covariance matrix, $\mathbf{C}^T$ , for PyV modulation 2. . . . . 40



27	Position of beam maps for computing $W_{lij}$ . . . . .	42
28	Diagonal window functions for MSAM-I with a Gaussian beam and with the true beam. . . . .	47
29	Effect of twist on the window functions. . . . .	48
30	Diagonal window functions with and without the flat sky ap- proximation. . . . .	54
31	Diagonal window functions for PyV. . . . .	55
32	Image of chopper offset constraint matrix. . . . .	59
33	Image of ground shield constraint matrix. . . . .	60
34	Getting limits from a likelihood curve. . . . .	62
35	PyV angular power spectrum constraints from the single mod- ulation analysis. . . . .	64
36	Histogram of $C_N N_{\text{files}}$ for a stare lag of zero. . . . .	66
37	Histogram of $C_N N_{\text{files}}$ for a stare lag of two. . . . .	67
38	$C_N N_{\text{files}}$ vs. stare lag. . . . .	67
39	Noise covariance matrix, $C^N$ , for mod 2. . . . .	68
40	Distribution of $\mathbf{C}^{-1/2} \vec{d}$ in the KL basis for modulation 7 using our best estimate noise matrix. . . . .	71
41	Distribution of $\mathbf{C}^{-1/2} \vec{d}$ in the KL basis for modulation 7 using a preliminary noise matrix. . . . .	72
42	$\chi^2/\text{dof}$ for each set using an expansion of the noise model of section 5.2. . . . .	74
43	$f(\Delta s)$ for set hb9. . . . .	76
44	$\mathbf{C}^M$ for set hb9, channel 45. . . . .	77
45	Angular power spectra obtained using 4 different noise models. . . . .	78
46	$\chi^2/\text{dof}$ for each set using the final noise matrix. . . . .	79
47	$\chi^2/\text{dof}$ for each set normalized to modulation 2. . . . .	80
48	PyV angular power spectrum constraints from the cross-modulation analysis. . . . .	82
49	Comparison of angular power spectra from single and cross- modulation analyses. . . . .	83
50	Weiner-filtered CMB and S/N maps for the main PyV region. . . . .	85
51	A comparison of PyV and PyIII maps. . . . .	86
52	Correlation coefficients and uncertainties for each foreground and modulation. . . . .	89
53	Upper limits on foreground contribution. All units are $\mu K$ . . . . .	90
54	CMB anisotropy measurements as of Feb 1999 with the PyV measurements overplotted. . . . .	92
55	PyV angular power spectrum and COBE-normalized standard CDM model. . . . .	93

## LIST OF TABLES

Table		Page
1	Python observing parameters. . . . .	11
2	Calibrations, efficiencies and corresponding uncertainties. . . . .	18
3	Observing sets. . . . .	24
4	Data cuts. . . . .	26
5	Instrument transfer function vs. mode. . . . .	30
6	Summary of analytic expressions for diagonal window functions for simple chopping strategies. . . . .	53
7	Angular power spectrum constraints from the single modulation likelihood analysis. . . . .	63
8	$\chi^2$ at best fit band power. Expected dof = $690 - 31 \times 2 = 628$ . . . . .	69
9	Angular power spectrum constraints from the cross-modulation analysis. . . . .	81
10	Correlation coefficients and uncertainties for weighted means. . . . .	89
11	Upper limits on foreground contribution. All units are $\mu K$ . . . . .	90

## ABSTRACT

Observations of the microwave sky using the Python telescope in its fifth season of operation at the Amundsen-Scott South Pole Station in Antarctica are presented. The system consists of a 0.75 m off-axis telescope instrumented with a HEMT amplifier-based radiometer having continuum sensitivity from 37-45 GHz in two frequency bands. With a  $0.91^\circ \times 1.02^\circ$  beam the instrument fully sampled 598 deg<sup>2</sup> of sky, including fields measured during the previous four seasons of Python observations. Interpreting the observed fluctuations as anisotropy in the cosmic microwave background, we place constraints on the angular power spectrum of fluctuations in eight multipole bands up to  $l \sim 260$ . The observed spectrum is consistent with both the COBE experiment and previous Python results. Total-power Wiener-filtered maps of the CMB are also presented. There is no significant contamination from known foregrounds. The results show a discernible rise in the angular power spectrum from large ( $l \sim 40$ ) to small ( $l \sim 200$ ) angular scales.

# CHAPTER 1

## INTRODUCTION

‘We know of an ancient radiation that haunts dismembered constellations, a faintly glimmering radio station.’

*Cake, Frank Sinatra*

The Cosmic Microwave Background Radiation (CMB), which formed when the universe was  $\sim 300,000$  years old (redshift  $z \sim 1100$ ), is the signature of a young, hot, dense universe. Along with big bang nucleosynthesis and the Hubble expansion, the CMB is one of the key observational pillars that support the big bang model of the universe.

Since its discovery (Penzias and Wilson 1965) and interpretation (Dicke et al. 1965), the CMB has been one of the most powerful tools for discriminating among cosmological models. The COBE satellite opened up a new era in CMB measurement, by detecting anisotropy on the largest scales with the DMR instrument (Smoot et al. 1992) and by establishing the blackbody nature ( $T=2.728 \pm 0.004$  K today) of the CMB spectrum to high precision with the FIRAS instrument (Mather et al. 1990, Fixsen et al. 1996). Measurement of anisotropy in the CMB directly probes conditions of the early universe. The anisotropies in the CMB are the seeds of the large scale

structures (galaxies, clusters of galaxies, and super-clusters) that we observe today. Observations of the angular power spectrum of CMB temperature fluctuations can be used to test theories of structure formation and constrain cosmological parameters.

There are three classes of measurements that could be made of the CMB: spectral, temperature anisotropy, and polarization anisotropy. This thesis describes a specific CMB temperature anisotropy experiment, Python V, with an emphasis on data reduction and analysis techniques. It is an expansion of Coble et al. (1999).

## 1.1 Theory

The theory of how CMB anisotropies grew via gravitational instability from primordial fluctuations is now well understood and has been discussed at length by other authors (see, for example, Hu et al. 1997). Before redshift  $z \sim 1100$ , photons and baryons were tightly coupled via Compton scattering, in a photon-baryon fluid. Acoustic oscillations in the fluid were created by the resistance of the photon pressure against gravitational compression. As the universe cooled, neutral hydrogen formed and radiation decoupled from matter and began free-streaming. The epoch of decoupling occurred at  $z \sim 1100$  for most cosmologies. Regions of compression and rarefaction in

the photon-baryon fluid at decoupling correspond to hot and cold spots that we observe in the CMB.

CMB angular power is usually expressed in terms of  $C_l$ 's. If the sky temperature is expanded as  $T(\theta, \phi) = \sum_{lm} a_{lm} Y_{lm}(\theta, \phi)$ , then the multipole moments,  $C_l$ , are defined as  $C_l = \langle |a_{lm}|^2 \rangle$ . Large  $l$  corresponds to small angular scales. Measuring the angular power spectrum of temperature anisotropies in the CMB is a powerful tool for determining many cosmological parameters, including the expansion rate of the universe ( $H_0$ ), the total density of the universe ( $\Omega$ ), the amount of baryonic matter ( $\Omega_b$ ) in the universe, the amount and nature of dark matter, the spectral index of primordial fluctuations ( $n$ ), the cosmological constant ( $\Lambda$ ), and the ionization history of the universe. Figure 1 shows the dependence of the angular power spectrum on various cosmological parameters.

Traditional cosmological tests, such as galaxy and cluster distributions, cannot probe these parameters directly, because they only determine the distribution of visible mass. They must assume an underlying bias, the unknown relation between mass and light, whereas CMB anisotropy corresponds directly to density fluctuations (White et al. 1994). CMB measurements are also independent of the extra-galactic distance ladder and probe parameters on a global scale.

As one example of the dependence of the CMB angular power spectrum on a cosmological parameter, the angular scale of the first acoustic peak (Figure 1) is a sensitive indicator of the total density,  $\Omega$ . The horizon scale at the epoch of decoupling, which corresponds to the scale of the first acoustic peak, is given by

$$\Delta\theta \approx 0.87^\circ \Omega^{1/2}. \quad (1.1)$$

As  $\Omega$  decreases, the peak occurs at smaller angular scales. For a flat universe ( $\Omega=1$ ), the corresponding angular scale is  $\sim 1^\circ$ .

## 1.2 Temperature Anisotropy Experiments

As with most astronomical measurements, CMB observations are usually conducted from locations inhospitable to humans, namely places that are high, dry, and cold, in order to reduce the interference from the atmosphere. CMB experiments have been and will be conducted from satellites, such as COBE, MAP (see the MAP website), and Planck (Planck website). The advantage to satellite missions is that they can map the whole sky with high precision and without interference from the atmosphere. The disadvantages are that they often have a long development period and are costly. A number of balloon-borne experiments have been conducted, such as ARGO (de Bernardis et al. 1994, Masi et al. 1996), BAM (Tucker et al. 1996),

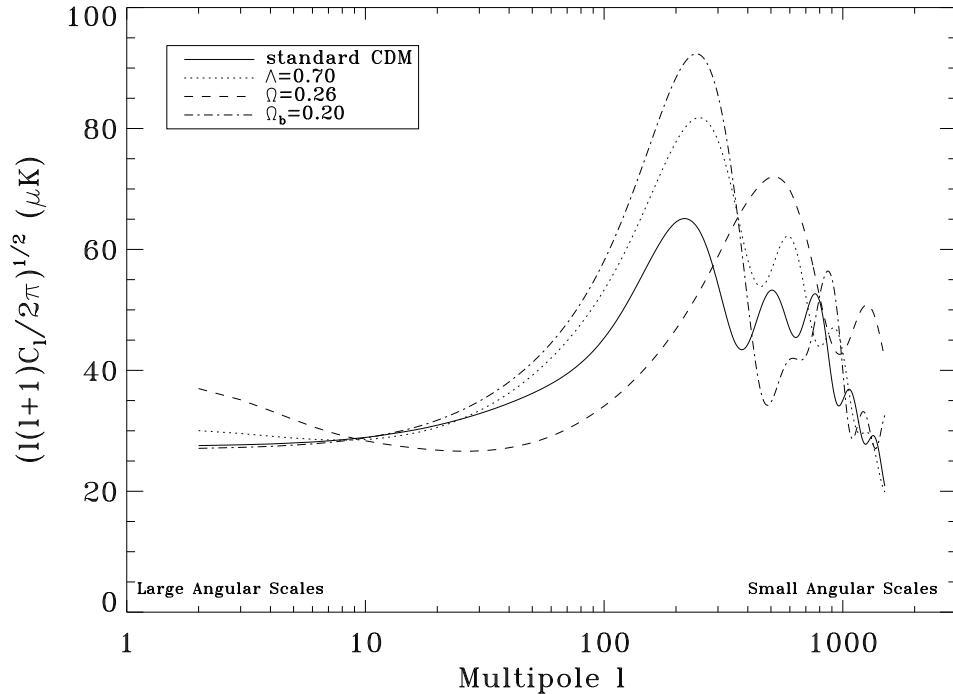


Figure 1 Model CMB angular power spectra for various cosmological parameters. Large  $l$  corresponds to small angular scales. Shown are a standard CDM model (solid line, density  $\Omega = 1.0$ , Hubble constant  $H_0 = 50$  km/s/Mpc, baryon density  $\Omega_b = 0.05$ , and cosmological constant  $\Lambda = 0.0$ ), a model with high baryon content (dot-dashed line,  $\Omega = 1.0$ ,  $H_0 = 50$  km/s/Mpc,  $\Omega_b = 0.20$ , and  $\Lambda = 0.0$ ), a model with a non-zero cosmological constant (dotted line,  $\Omega = 1.0$ ,  $H_0 = 50$  km/s/Mpc,  $\Omega_b = 0.02$ , and  $\Lambda = 0.70$ ), and an open model (dashed line,  $\Omega = 0.26$ ,  $H_0 = 50$  km/s/Mpc,  $\Omega_b = 0.06$ , and  $\Lambda = 0.0$ ). The models were computed using CMBFAST (Seljak and Zaldarriaga 1996).

FIRS (Ganga et al. 1994), MAX (Lim et al. 1996, Tanaka et al. 1996), MSAM (Cheng et al. 1997), and QMAP (Devlin et al. 1998, Herbig et al. 1998). These balloon flights typically observe the sky for one night per year. The next generation of balloon-borne experiments, long-duration ballooning (LDB) experiments, are currently under way. The BOOMERANG



(BOOMERANG website) experiment circumnavigated Antarctica, observing for approximately 10 days in December 1998. The TopHat (TopHat website) experiment is scheduled for an LDB flight in December 1999. A plethora of experiments have detected or constrained CMB anisotropy from the ground. The South Pole is an especially attractive site for CMB measurement because of its stable atmosphere and high altitude. The Python (Dragovan et al. 1994, Ruhl et al. 1995, Platt et al. 1997, Kovac et al. 1999), Viper (Peterson et al. 1998), and ACME (Gaier et al. 1992, Schuster et al. 1993, Gundersen et al. 1995) telescopes have made observations from the South Pole. Other ground-based experiments include CAT (Scott et al. 1996), IAB (Piccirillo and Calisse 1993), IAC (Femenia et al. 1997), MAT (Torbet et al. 1999), OVRO NCP (Readhead et al. 1989), OVRO RING5M (Leitch et al. 1998), Saskatoon (SK) (Netterfield et al. 1996), SuZIE (Church et al. 1997) and Tenerife (Hancock et al. 1997).

Since anisotropies are temperature differences, CMB experiments must difference (chop) in some way. The chopping, whether internal or external, must be quick, and come back to the same place on the sky faster than the  $1/f$  noise in the electronics and atmosphere. Often this is accomplished with a chopping secondary mirror (the chopper) and/or an internal Dicke switch. Some simple chopping strategies include a single difference (2-point chop), for which  $\Delta T_i = T_{i+1} - T_i$ , a double difference (3-point chop), for which

$\Delta T_i = T_i - \frac{1}{2}T_{i-1} - \frac{1}{2}T_{i+1}$ , and a 4-point chop, for which  $\Delta T_i = -\frac{1}{4}T_i + \frac{3}{4}T_{i+1} - \frac{3}{4}T_{i+2} + \frac{1}{4}T_{i+3}$ . Other experiments perform a continuous (fast) scan with the chopper and modulate the data in software, scan slowly with the telescope and read out the detectors quickly, or spin rapidly. Chopping strategies are sometimes called lockins, harmonics, modulations, or demodulations.

There are 2 basic detector technologies used for CMB experiments: bolometers and HEMTs. SIS detectors are also sometimes used. HEMTs have the advantage that they are robust and easy to use. They are inherently polarization sensitive, coherent detectors that typically operate at frequencies  $\lesssim 90$  GHz. They can operate at room temperature, but become more sensitive as they are cooled down to  $\sim 10$  K. Bolometers are more sensitive than HEMTs, but they are less robust and must be cooled to at least 0.25 K, so much work must go into the cryogenics. Bolometers typically operate at frequencies  $\gtrsim 90$  GHz and are often used on balloon-borne experiments, where their sensitivity is better than the atmospheric noise. It is advantageous to make measurements at several frequencies in order to spectrally distinguish possible contamination by galactic foregrounds (e.g. dust, synchrotron).

CMB anisotropies can also be measured using interferometers, such as CAT, which has detected anisotropy, DASI (White et al. 1997), which will observe at large to medium angular scales from the South Pole, and CBI (CBI website), which will observe at small angular scales from Chile. Inter-

ferometers are advantageous because they have low systematics.

In choosing an observing strategy (how much time to spend on which region of the sky and in what order), the theoretically optimal signal-to-noise ratio  $S/N=1$ , is too optimistic. In reality, experiments should have  $S/N>1$ , in order to perform consistency checks on the data. Interlaced observing strategies are desirable because they reduce striping in the maps obtained, but that is not always possible given observing sites and conditions.

Results from the COBE satellite (Smoot et al. 1992) tightly constrain the angular power spectrum at the largest angular scales. Several experiments have measured the angular power spectrum at degree angular scales (e.g., SP, MAX, Python I-IV, MSAM, SK, QMAP). Figure 2 is a compilation of measurements of the angular power spectrum previous to the publication of the PyV measurements. Collectively the data show a rise in power towards smaller angular scales; individually no experiment covers a wide range of angular scales from COBE scales to degree scales, and most cover only small regions of the sky.

The dataset from the fifth Python observing season (hereafter PyV) has sufficient sky coverage to probe the smallest scales to which COBE was sensitive, while having a small enough beam to detect the rise in angular power at degree angular scales.

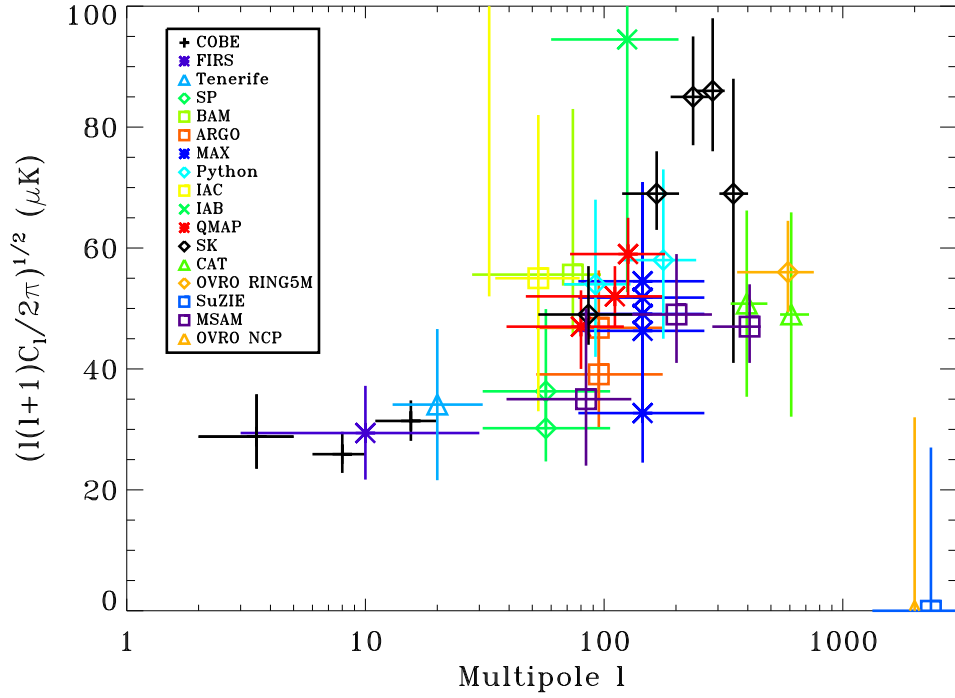


Figure 2 CMB anisotropy measurements as of Feb 1999. The points are COBE (Hinshaw et al. 1996), FIRS (Ganga et al. 1994), Tenerife (Hancock et al. 1997), SP (Gundersen et al. 1995), BAM (Tucker et al. 1996), ARGO (de Bernardis et al. 1994, Masi et al. 1996), MAX (Tanaka et al. 1996), Python I-III (Platt et al. 1997), IAB (Piccirillo and Calisse 1993), IAC (Femenia et al. 1997), QMAP (de Oliveira-Costa et al. 1998), SK (Netterfield et al. 1996), CAT (Scott et al. 1996), OVRO RING5M (Leitch et al. 1998), SuZIE (Church et al. 1997), MSAM (Wilson et al. 1999), and OVRO NCP (Readhead et al. 1989).

## CHAPTER 2

### THE PYTHON EXPERIMENT

‘Python is a large non-venomous Old World snake that coils around and suffocates its prey.’

Oxford American Dictionary

#### 2.1 Introduction to the Python Experiment

In its first four seasons the Python experiment detected significant anisotropy in the CMB (Dragovan et al. 1994 (PyI), Ruhl et al. 1995 (PyII), Platt et al. 1997 (PyIII), Kovac et al. 1999 (PyIV)). Observations from the first three seasons were made at 90 GHz with a bolometer system and a 4-point chop scan strategy, yielding CMB detections at angular scales of  $l \sim 90$  and  $l \sim 170$ . During the PyIV season measurements were made using the same scan strategy with a HEMT amplifier-based radiometer, confirming PyI-III detections in a 37-45 GHz frequency band.

Observations were made from November 1996 through February 1997 in the fifth Python observing season. In order to increase the range of observed angular scales, a smoothly scanning sampling scheme was implemented. As

Season	dates	$\nu_c$	FWHM	chop	throw	$l_{eff}$	fields
PyI	12/92	90.3	0.82°	4-pt	8.25°	87	15
PyII	12/93	90.3	0.82°	4-pt	8.25°	87	31
PyIII-L	10/94-12/94	90.3	0.82°	4-pt	8.25°	87	110
PyIII-S	10/94-12/94	90.3	0.82°	4-pt	2.75°	170	140
PyIV	2/96	40.1	1.06°×1.12°	4-pt	8.25°	85	14
PyV	11/96-2/97	40.3	0.91°×1.02°	triangle	11.0°	40-260	598 deg <sup>2</sup>

Table 1 Python observing parameters (adapted from Kovac et al. 1999).  $\nu_c$  is the central frequency of the observations, FWHM is the FWHM of the beam, chop is the chopping strategy, throw is the extent of the chopper sweep,  $l_{eff}$  is the multipole (angular scale) at which observations were made, and fields is the number of fields observed or the sky coverage.

a result, PyV is sensitive to the CMB angular power spectrum from  $l \sim 40$  to  $l \sim 260$ .

Table 1 summarizes the observing parameters from all five Python seasons.

## 2.2 Instrument

The PyV measurements were made using the same receiver as the PyIV system as described in Alvarez (1996) and Kovac et al. (1999). A schematic of the receiver is shown in Figure 3. The receiver consists of two focal-plane feeds, each with a single 37-45 GHz HEMT amplifier. A diplexer splits each signal at  $\sim 41$  GHz before detection, giving four data channels. The analysis reported here eventually combines signals from all four channels, resulting in

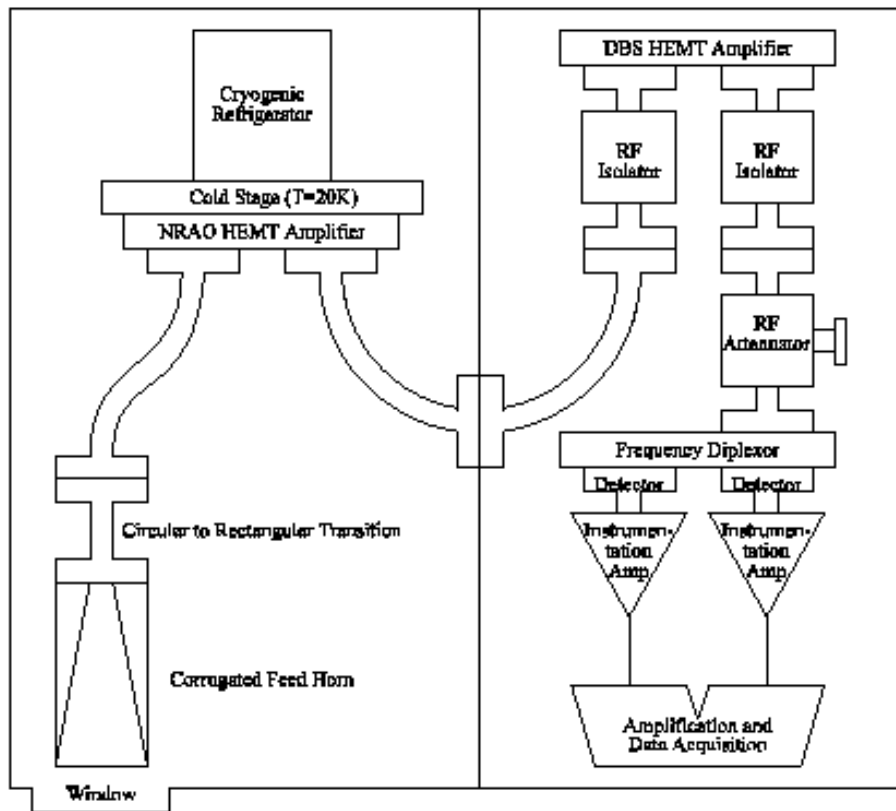


Figure 3 Schematic diagram of the receiver (Alvarez 1996). The signal path is shown for only one of the two feeds.

a thermal radiation centroid  $\nu_c = 40.3$  GHz and effective passband  $\Delta\nu = 6.5$  GHz for the PyV dataset. The bandpasses for the four data channels are shown in Figure 4.

The receiver is mounted on a 0.75 m diameter off-axis parabolic telescope (Dragovan et al. 1994), which is surrounded by a large ground shield to block stray radiation from the ground and Sun. The beams corresponding to the two feeds observe the same elevation and are separated by  $2.80^\circ$  on

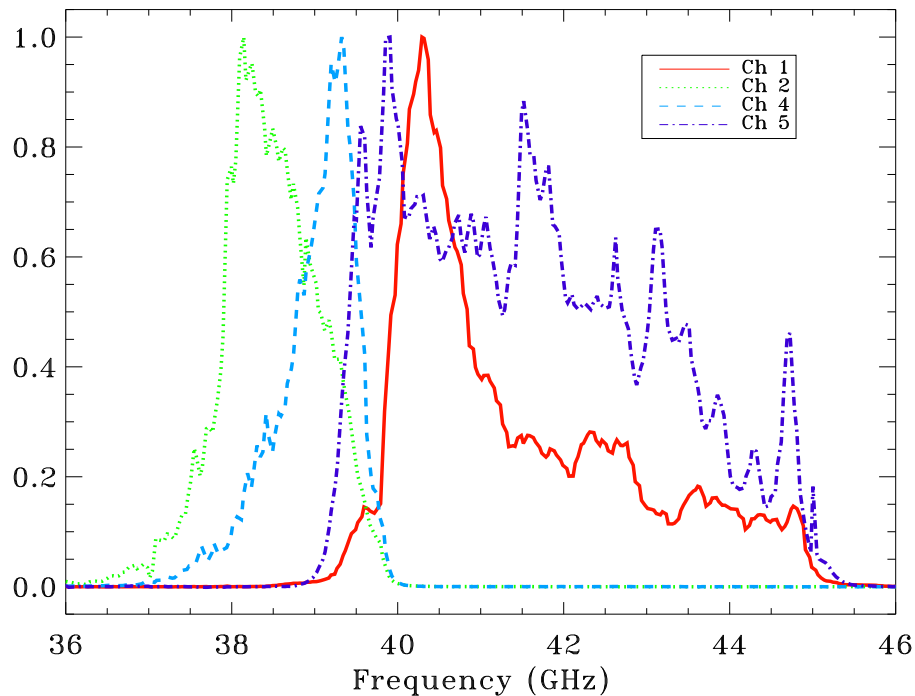


Figure 4 Bandpasses for the 4 data channels. Channel 3 is a dark channel. Channels 1 and 2 observe the same points on the sky as do channels 4 and 5. The bandpasses are similar in frequency range, so that the reduced data from channels which observe the same points on the sky are eventually co-added (Chapter 3).

the sky. These beams are scanned horizontally across the sky by a large rotating vertical flat mirror, the chopper, at 5.1 Hz. The new scan strategy motivated two changes from the instrument configuration described in Kovac et al. (1999): the frequency response of the data system was extended by switching to 100 Hz-rolloff antialiasing Bessel filters, and the data recording rate was correspondingly increased, to 652.8 samples/sec for each channel.

A schematic of the telescope is shown in Figure 5. Pictures of the telescope



with and without the ground shield are shown in Figures 6 and 7 respectively.

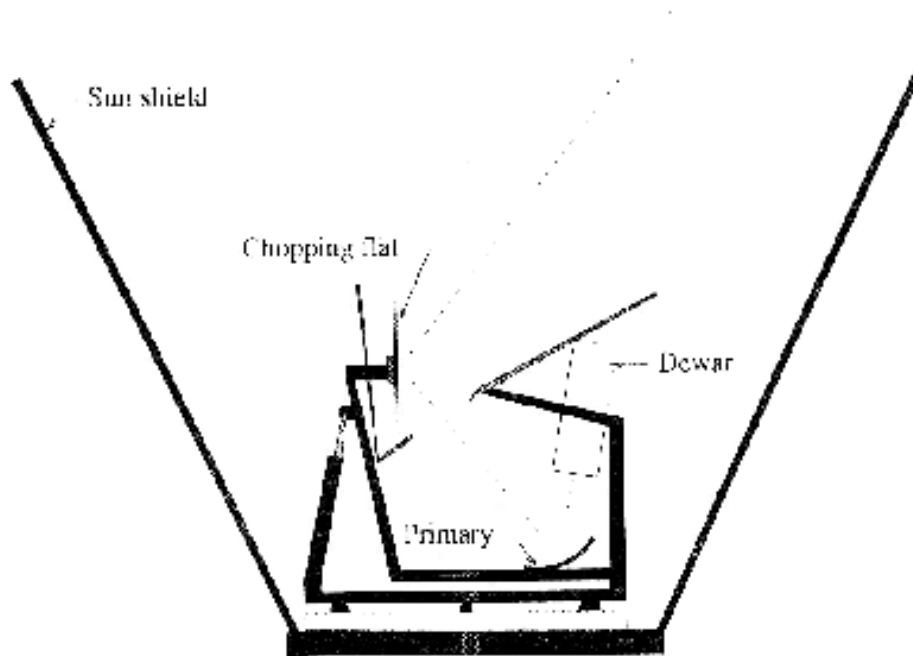


Figure 5 Schematic diagram of the Python telescope (Dragovan et al. 1994). The telescope is surrounded by a large ground/Sun shield. The chopping flat (chopper) is oriented vertically and scans in azimuth.

### 2.3 Calibration

As in previous Python seasons, the primary DC calibration of the detectors was derived using liquid nitrogen, liquid oxygen, and ambient temperature thermal loads external to the receiver (Dragovan et al. 1994, Ruhl et al. 1995). Load calibrations were performed approximately once per day, and gains were found to be consistent over the entire season to within  $\pm$



Figure 6 Picture of the Python telescope without the ground shield or dewar. For CMB observations the telescope is oriented such that the chopper is vertical.



Figure 7 A view of the Python telescope and surrounding labs.

2%, with no discernible trends. Gain compression, which was a source of systematic uncertainty in the calibration of PyI-PyIII, is measured to be negligible for the Python HEMT receiver. Systematic uncertainty in the DC load calibration is estimated to be  $\pm 10\%$ .

Several efficiencies must be estimated to relate the load calibrations to celestial response in the main beam, which account for power losses in the atmosphere, in the sidelobes, and in the telescope, and they are calculated using data from skydips and from various beam measurements. In order to account for the net effect of atmospheric attenuation and beam efficiency, the data must be multiplied by a factor of 1.10. The resulting systematic calibra-

tion uncertainty of  $\begin{smallmatrix} +10\% \\ -4\% \end{smallmatrix}$  is asymmetric, due to the fact that the individual losses are small positive numbers and hence the errors in their estimation follow skewed distributions (Kovac et al. 1999).

The dynamic response of the system was calculated from laboratory measurements of the transfer functions for the AC coupling and antialiasing filters in the data system, and confirmed on the telescope by comparison of observations made of the moon using normal and slow chopper speeds. The response speed of the detectors is not a concern for this calibration or for its uncertainty. An appropriate response correction factor is applied to each modulation of the data. The uncertainty on these factors is small, and is dominated by a  $\pm 5\%$  systematic uncertainty on their common normalization.

The overall uncertainty in the calibration of this dataset is estimated to be  $\begin{smallmatrix} +15\% \\ -12\% \end{smallmatrix}$ . Antenna temperature has been converted to units of  $\delta T_{\text{CMB}}$  throughout. The calibrations, efficiencies and their uncertainties are summarized in Table 2.

## 2.4 Observations

Observations for the PyV season were taken from November 1996 through February 1997.

Calibration	Uncertainty (%)
DC load systematic	$\pm 10$
DC load statistical	$\pm 2$
atmospheric attenuation plus beam efficiency	+10, -4
dynamic response	$\pm 5$
<b>TOTAL</b>	<b>+15, -12</b>

Table 2 Calibrations, efficiencies and corresponding uncertainties.

### 2.4.1 Observing Regions

Two regions of sky were observed: the PyV main field, a  $7.5^\circ \times 67.7^\circ$  region of sky centered at  $\alpha = 23.18^h$ ,  $\delta = -48.58^\circ$  (J2000) which includes fields measured during the previous four seasons of Python observations and a  $3.0^\circ \times 30.0^\circ$  region of sky centered at  $\alpha = 3.00^h$ ,  $\delta = -62.01^\circ$  (J2000), which encompasses the region observed with the ACME telescope (Gundersen et al. 1995). The total sky coverage for the PyV regions is 598 deg<sup>2</sup>, greater sky coverage than previous degree-scale CMB experiments. Figure 8 shows the IRAS 100  $\mu m$  view of the galaxy with the Python observing regions superimposed.

### 2.4.2 Observing Strategy

Both PyV regions are fully sampled with a grid spacing of  $0.92^\circ$  in elevation and  $2.5^\circ$  in right ascension, corresponding to a distance of  $1.6^\circ$  on the

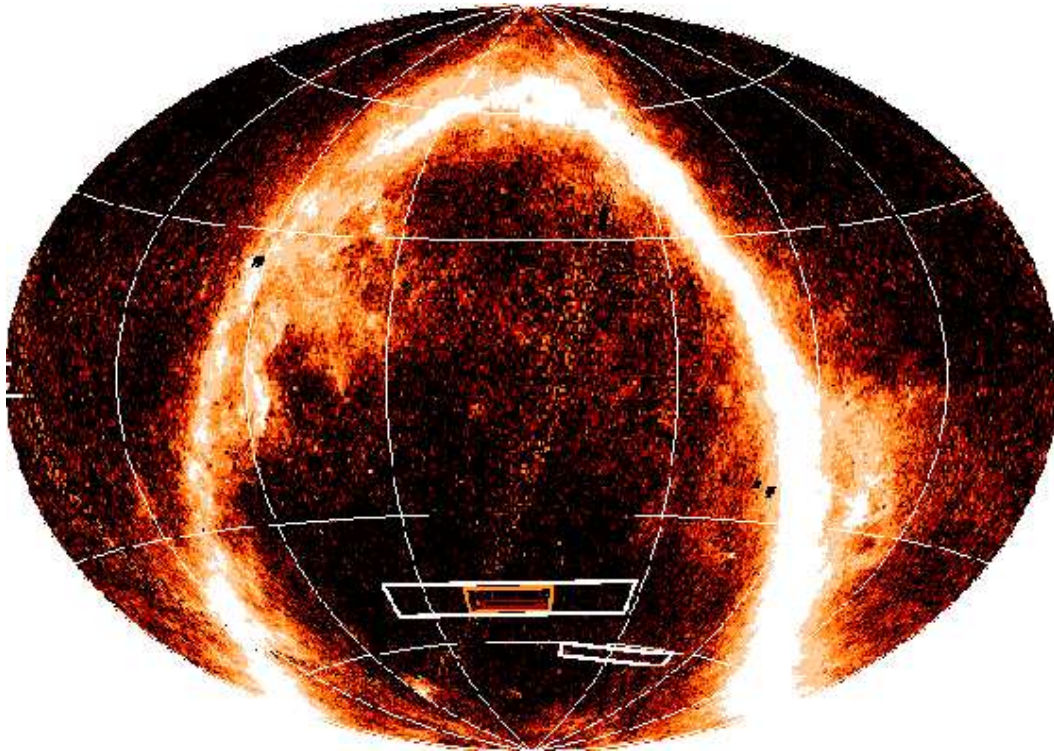


Figure 8 IRAS  $100\ \mu\text{m}$  view of the galaxy with the Python observing regions superimposed. The 2 large white boxes indicate the PyV regions, the medium-sized orange box PyIII, and the small red box PyIV. This demonstrates the large sky coverage achievable from the South Pole in one of the most clean regions of sky.

sky at a declination of  $-50^\circ$ . A grid of the center positions of the PyV fields is shown in Figure 9. The telescope is positioned on one of the fields and the chopper smoothly scans the beams in azimuth in a nearly triangular wave pattern (Figure 10). The chopper throw is  $17^\circ$  in azimuth, corresponding to  $11^\circ$  on the sky at a declination of  $-50^\circ$ . The telescope tracks on each field; it does not drift scan.

There are 128 data samples for each detector channel in a complete chop-

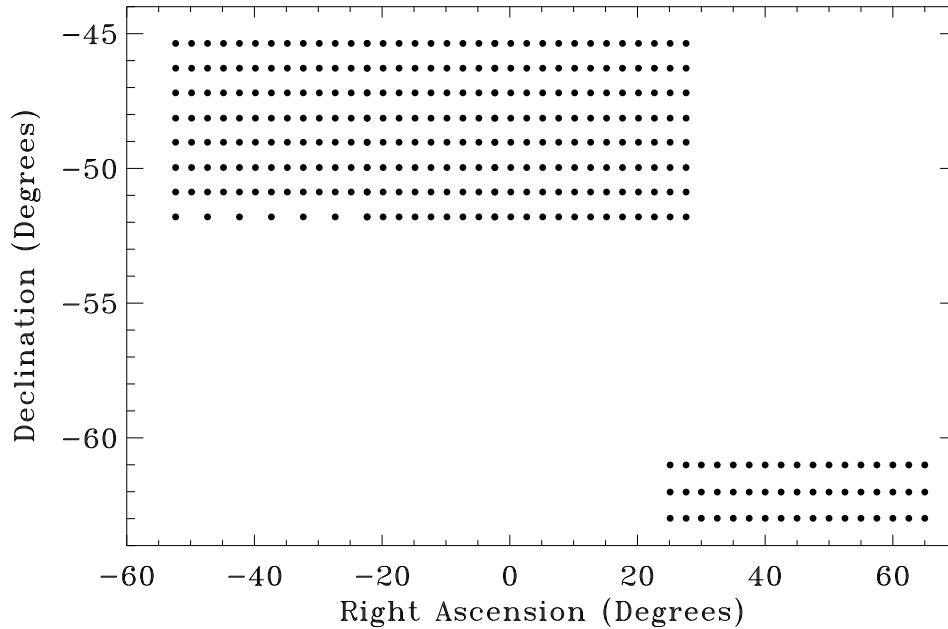


Figure 9 Center positions of the Python V fields. The fields are  $2.5^\circ$  apart in right ascension, which corresponds to  $1.6^\circ$  on the sky at a declination of  $-50^\circ$ . The fields are  $0.92^\circ$  apart in declination.

per cycle, and 164 chopper cycles ( $\sim 32$  s) of data (one stare) are taken of a given field before the telescope is positioned on the next field in the set. One data file consists of 164 chopper cycles for each field in the set. For a set which contains 13 fields, one data file is  $\sim 32$  s  $\times$  13  $\sim 6.9$  min long.

Approximately 13 hours of good data (100 files) are taken of a set of fields before the telescope moves on to the next set of fields. A total of 309 fields are observed in 31 sets of 5–17 fields. Some fields are observed in more than one set, yielding 345 effective fields. Figure 11 labels the observing sets with respect to the grid shown in Figure 9 and Table 3 lists the number of

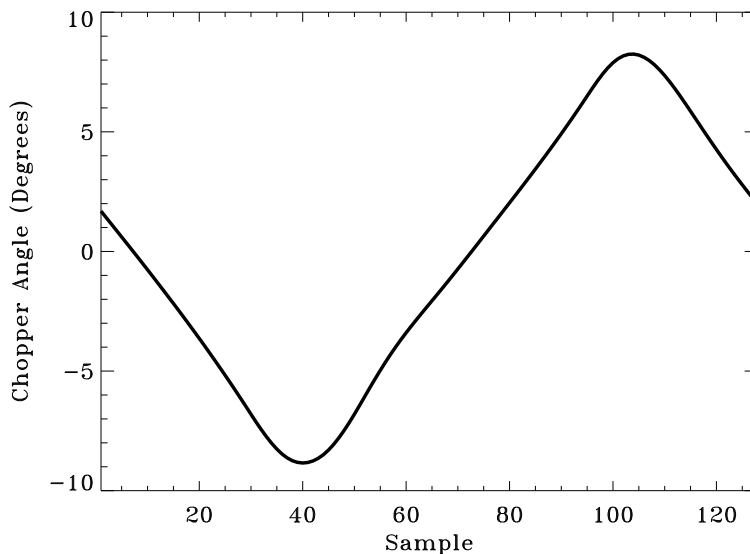


Figure 10 Motion of the chopper. The chopper smoothly scans in azimuth in a nearly triangular wave pattern at 5.1 Hz. The waveform is not perfectly triangular because the chopper slows down when turning around and because the LVDT is non-linear.

fields in each set, the number of files of good data taken in each set, and the declination at which each set was taken.

### 2.4.3 Pointing

The combined absolute and relative pointing uncertainty is estimated to be  $0.15^\circ$ , as determined by measurements of the moon and the Carinae nebula ( $\alpha = 10.73h, \delta = -59.65^\circ$ ). The beams corresponding to the 2 feeds observe the same elevation and are separated by  $2.80^\circ$  on the sky (Figure 12).



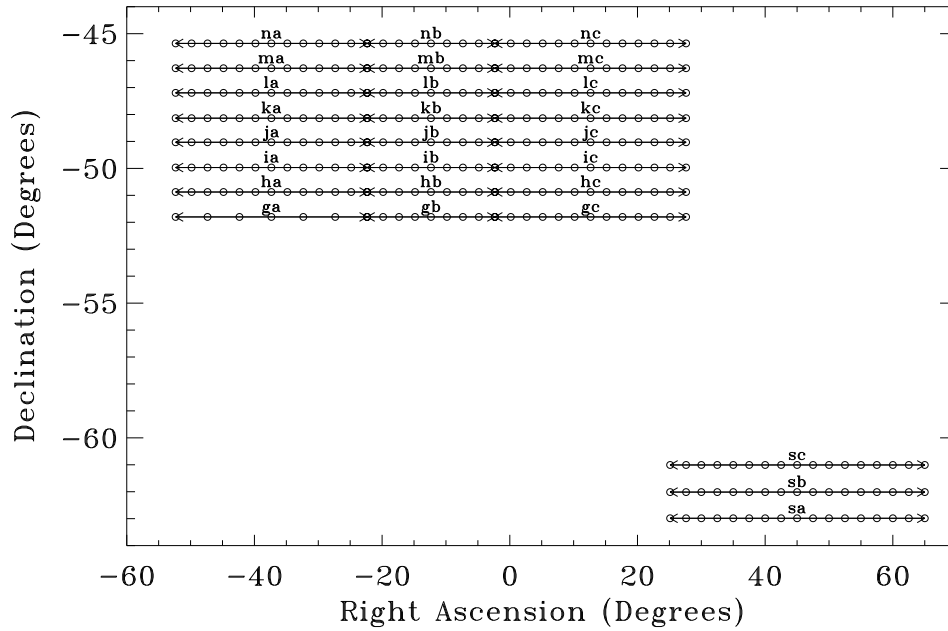


Figure 11 Observing sets. Each set is observed for approximately a day (leaving  $\sim 13$  hours of good data) before moving on to the next set. Neighboring sets in the main PyV region overlap by 1 field. Circles represent the fields and arrows point to the end fields in each set. In addition to the sets shown, sets *ib*, *jb*, *kb*, and *lb* were observed with a scan pattern of 5 fields per file.

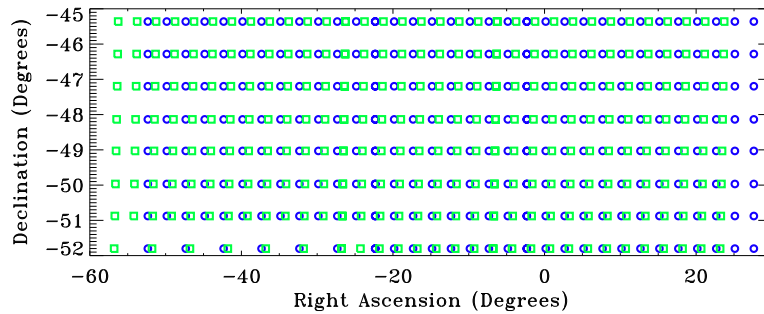


Figure 12 Pointing of the two feeds on the sky in the main PyV region. The beams corresponding to the two feeds observe the same elevation and are separated by  $2.80^\circ$  on the sky. The squares represent the positions of channels 1 and 2 and the circles represent the positions of channels 4 and 5.

#### 2.4.4 *Beam*

The beam is determined from scans of the Carinae nebula and the Moon. Scans of the Carinae nebula were obtained from the Viper telescope (Griffin and Peterson 1998), which has the same receiver system as PyV and a  $0.25^\circ$  beam. The Viper scans were convolved with asymmetric Gaussian beams of widths  $\sigma_x$  and  $\sigma_y$ . The widths were varied as free parameters and best fits to the observed PyV beams were obtained. This convolution procedure works better than a deconvolution procedure because of the noise in the measurements. The results are not dependent on size of the Carina nebula assumed in the fits. The PyV beam is well approximated by an asymmetric Gaussian of FWHM  $0.91_{-0.01}^{+0.03} \times 1.02_{-0.01}^{+0.03}$  degrees ( $az \times el$ ).

Set	$N_{\text{fields}}$	$N_{\text{files}}$	$\delta$
sa	17	41	-62.99
sb	17	103	-62.01
sc	17	33	-61.01
ga	7	302	-51.80
gb	9	184	-51.80
gc	13	95	-51.80
ha	13	100	-50.88
hb	9	84	-50.88
hc	13	104	-50.88
ia	13	45	-49.97
ib	9	130	-49.97
ib	5	52	-49.97
ic	13	119	-49.97
ja	13	120	-49.03
jb	9	269	-49.03
jb	5	250	-49.03
jc	13	109	-49.03
ka	13	81	-48.14
kb	9	186	-48.14
kb	5	295	-48.14
kc	13	59	-48.14
la	13	191	-47.20
lb	9	298	-47.20
lb	5	343	-47.20
lc	13	122	-47.20
ma	13	113	-46.28
mb	9	198	-46.28
mc	13	124	-46.28
na	13	153	-45.36
nb	9	50	-45.36
nc	13	107	-45.36

Table 3 Observing sets.

## CHAPTER 3

### DATA REDUCTION

#### 3.1 Data Cuts

A total 719.52 hours of data were taken during the PyV season. After cutting 45.6% of the data for file errors, tracking errors and weather, 391.32 hours of data remained for use in the CMB analysis. Table 4 summarizes the data cuts.

A file is cut:

- for file errors if any of the data, pointing, or time matrices are empty, if the time matrices from the two data computers did not agree, or if the number of stares in the data, pointing and time matrices did not agree.
- for a relative pointing error if the stare that is furthest from where it should be relative to the scan center is more than 3' from where it should be.
- for an absolute pointing error if its scan center deviates by more than 6' from the scan center of all other files in the set.

Cut	hours	percent
internal file errors	10.42	1.45
relative pointing	49.39	6.86
absolute pointing	73.43	10.21
chopper error	7.47	1.04
low levels	24.48	3.40
high levels	163.01	22.65
<b>TOTALCUTS</b>	<b>328.20</b>	<b>45.61</b>

Table 4 Data cuts.

- if the mean chopper waveform in any stare deviates by more than 1% from the benchmark waveform made from the whole data set.
- for anomalously low noise levels, which could be caused by the power failing and the dewar heating up or the gain being set to the wrong level.
- for anomalously high noise levels, which are caused by weather. There is a clear distinction between good and bad weather.

## 3.2 Modulations

The data are modulated using

$$M_m(\theta) = \cos(m\pi\theta/\theta_c) \times \begin{cases} 1 & m = 1 \\ H(\theta) & m = 2 \dots 8 \end{cases} \quad (3.1)$$

where  $m$  is the modulation number,  $\theta$  is the chopper angle,  $\theta_c$  is the extent of the chopper throw and  $H(\theta) = 0.5(1 - \cos(2\pi\theta/\theta_c))$  is a Hann window (Figure 13). The  $m = 2 \dots 8$  modulations are apodized with the Hann window in order to reduce the ringing of the window functions in  $l$ -space. Data taken during the right- and left-going portions of the chopper cycle are modulated separately, to allow for cross-checks of the data. Sine modulations are not used in the analysis because they are anti-symmetric and are thus sensitive to gradients on the sky.

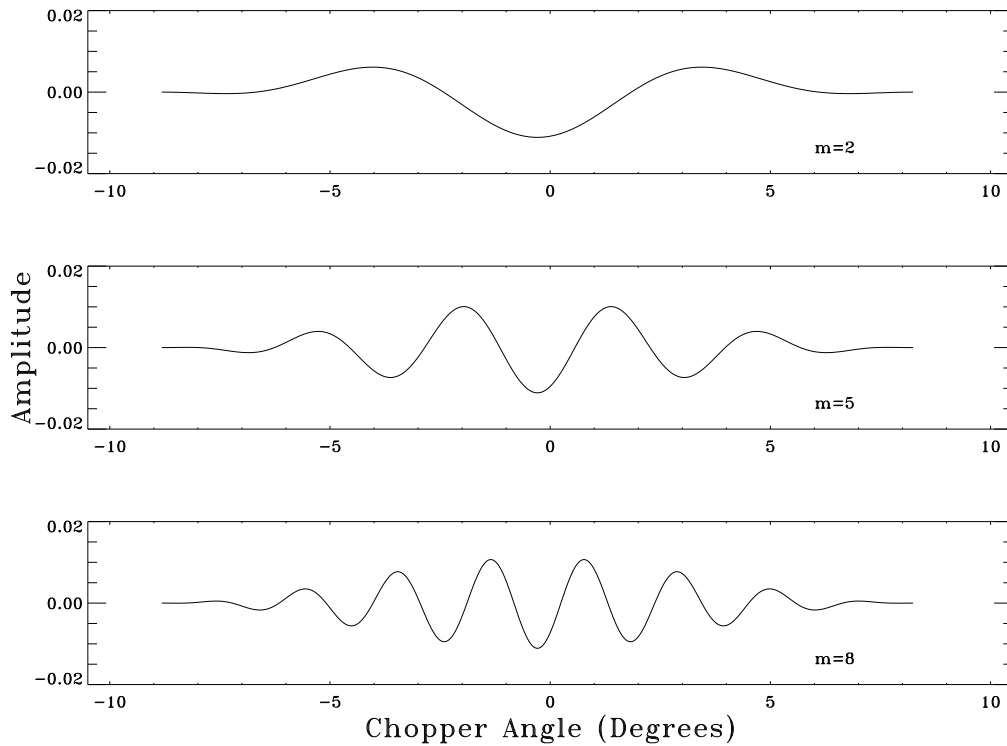


Figure 13 The data are modulated with cosines which have been apodized by a Hann window. Three of the modulations are shown.

The modulations in equation 3.1 and Figure 13 are cosines or apodized

cosines in space, not in time. Since the chopper waveform (Figure 10) is non-linear, the timestream modulations are not strictly cosines or apodized cosines in time (or chopper sample). Rather, they are created to produce the spatial response in equation 3.1 and Figure 13. The timestream modulations as a function of chopper sample are shown in Figure 14. The timestream modulations,  $M_m(s)$  are normalized such that  $\sum_s M = 0$  (so that a uniform temperature does not contribute) and  $\sum_s |M| = 2$  where  $s$  is chopper sample, following the single difference convention.

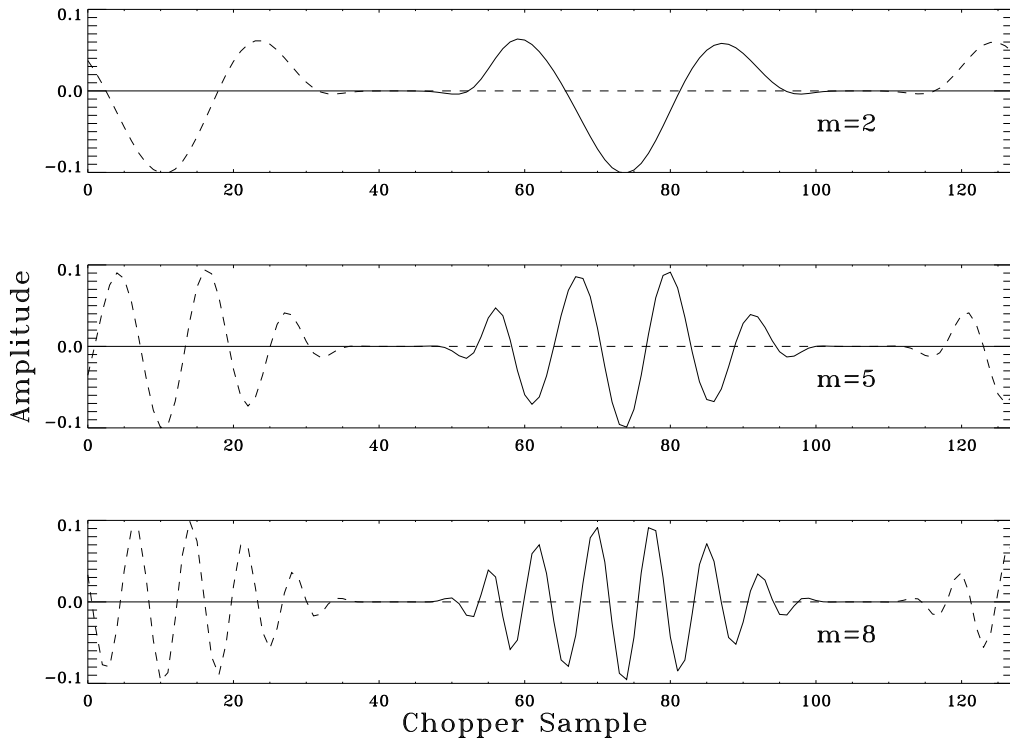


Figure 14 Timestream modulations. Since the chopper waveform is non-linear, the timestream modulations are created so that the spatial response will be cosines or apodized cosines. These 3 timestream modulations correspond to the 3 spatial modulations shown in Figure 13.

### 3.3 Instrument Transfer Function

The instrument transfer function produces two main effects on the data: a roll-off with frequency and a phase shift between data taken during the right and left-going portions of the chopper cycle (hereafter right and left data). Figure 15 shows the frequency dependence of the transfer function. Since each modulation is well-isolated in frequency space, the effect of the

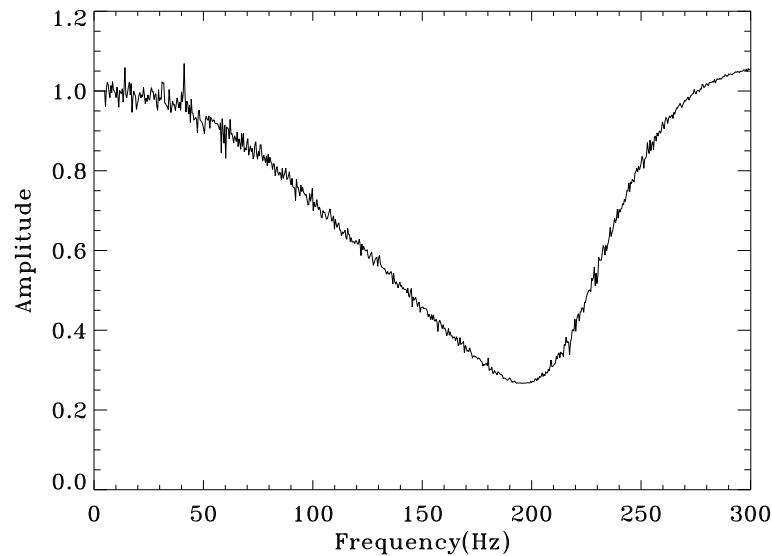


Figure 15 Frequency dependence of the instrument transfer function.

frequency roll-off of the transfer function can be accounted for with 1 number for each modulation (Table 5). The modulated data are divided by  $T$  to remove the frequency dependence of the transfer function.

Figure 16 shows the phase effect of the transfer function on right and left unmodulated moon data and Figure 17 shows modulated moon data, in



mode	$f$ (Hz)	$T$
1	13	1.0
2	22	.99
3	33	.98
4	43	.95
5	55	.92
6	66	.88
7	77	.83
8	88	.79

Table 5 Instrument transfer function vs. mode. Frequency  $f$  is the peak frequency of each modulation.

which right and left data are properly phased. If the right and left data are not properly phased, the signal will be washed out.

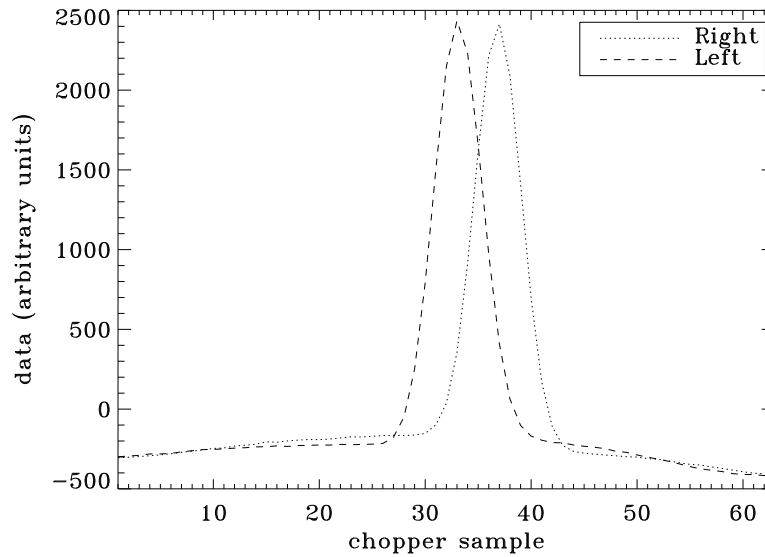


Figure 16 Unmodulated moon data showing effect of the transfer function on the right-left phase. Data from one stare and channel is shown as an example.

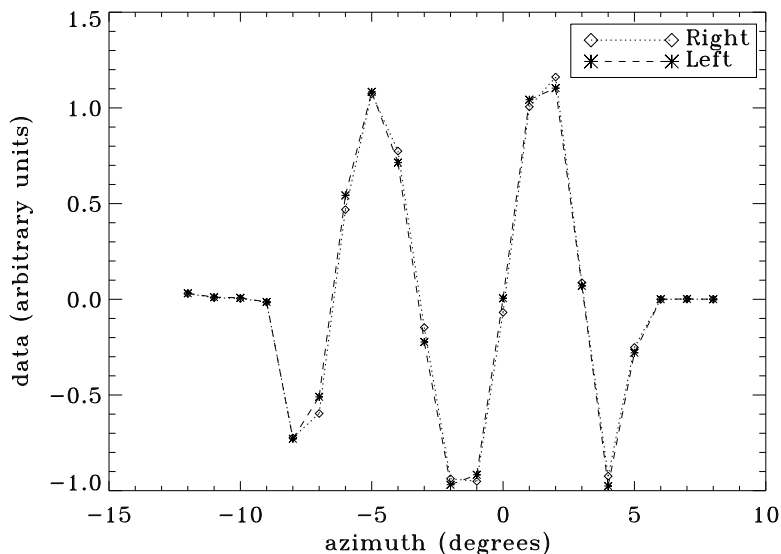


Figure 17 Checking the phase of right and left data on the moon. Data from channel 1, modulation 3 is shown as an example. If the right and left data are not properly phased, the signal will be washed out.

### 3.4 Chopper Synchronous Offset

Data in a given file, field, channel, and modulation are co-added over all chopper cycles. A chopper synchronous offset, caused by differential spillover past the chopper, is removed from each data file by subtracting the average of all of the fields in a file. This is not just a DC offset; there is an offset removed for each modulation (or equivalently, for each sample of the chopper waveform) and channel. Figure 18 shows the chopper offset as a function of time for one of the channels and modulations as an example. Figure 19 shows a histogram of the chopper offset for that same channel and modulation. The large scatter in both figures is due to noise.

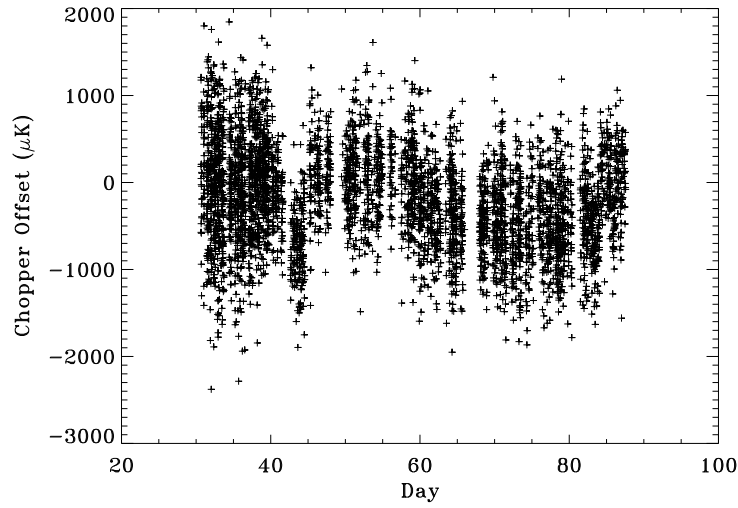


Figure 18 Chopper offset vs. time for channel 1, modulation 2, right-going data. Each point corresponds to the offset removed from one file.

To test that the chopper offset is stable over a file, we take the difference in chopper offset between two adjacent files in time. A plot of the chopper

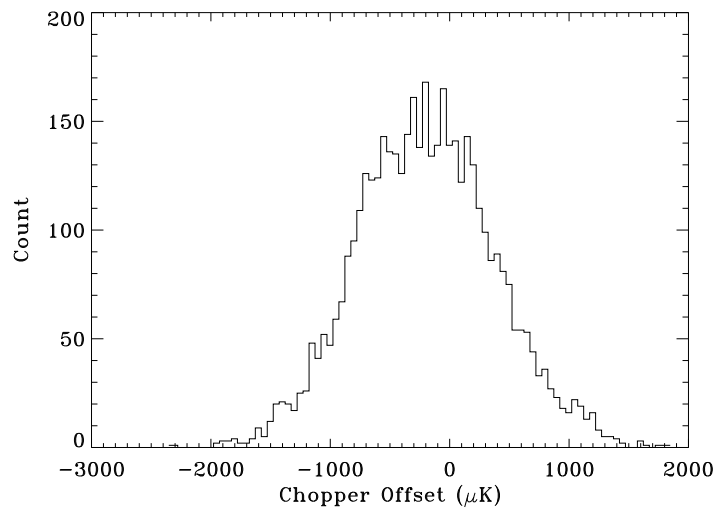


Figure 19 Histogram of chopper offset for channel 1, modulation 2, right-going data.

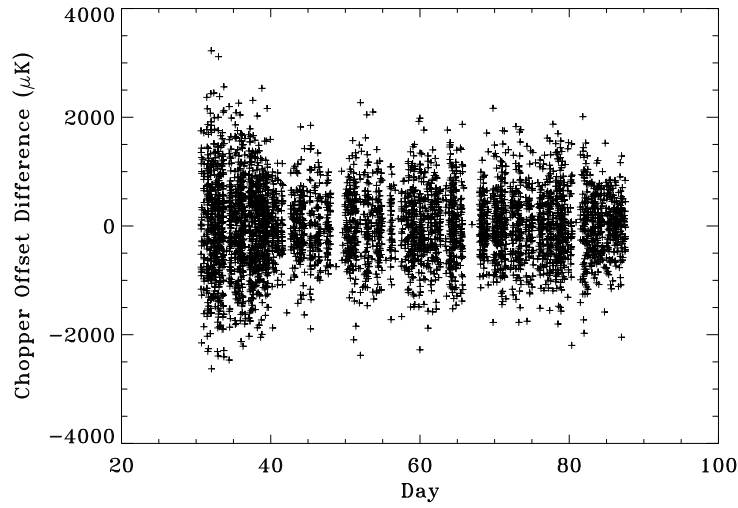


Figure 20 Chopper offset difference vs. time for channel 1, modulation 2, right-going data. Each point corresponds to the offset difference between adjacent files in time.

offset difference is shown in Figure 20 and a histogram is shown in Figure 21. Again, there is a large scatter due to noise.

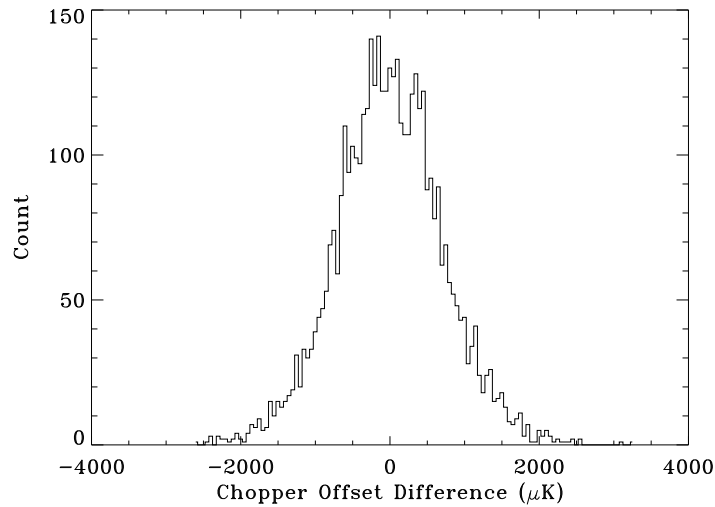


Figure 21 Histogram of chopper offset difference for channel 1, modulation 2, right-going data.

In order to compare the size of the chopper offset and the chopper offset difference with the scatter due to noise reduced, we compute the mean chopper offset and mean chopper offset difference for each channel and modulation over the whole data set. As illustrated in Figures 22 and 23, the chopper offset difference is significantly smaller (by at least 3 orders of magnitude) than the chopper offset. Further, when the differencing procedure is repeated as a function of file lag, the results indicate that the chopper offset is stable over  $\sim 5$  files. Thus our assumption that the chopper offset is stable over 1 file is a correct and even a conservative assumption.

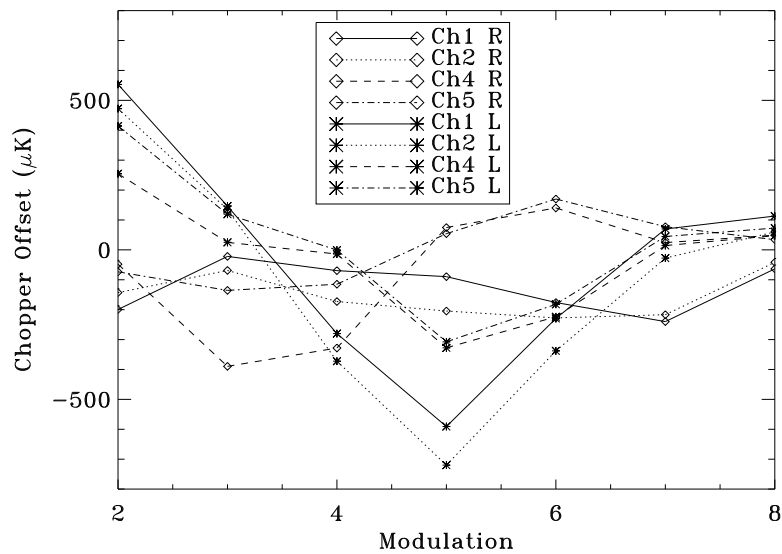


Figure 22 Mean chopper offset over the data set for all channels, right and left-going data vs. modulation. A different chopper offset is subtracted from each file.

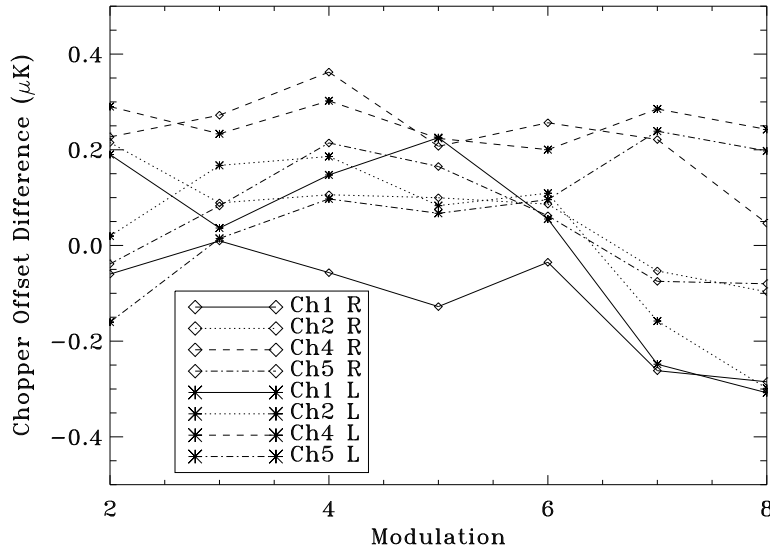


Figure 23 Mean chopper offset difference over the data set for all channels, right and left-going data vs. modulation. The chopper offset difference is significantly smaller than the chopper offset (Figure 22), indicating that the chopper offset is stable over a file. The vertical scale in this figure covers a smaller range than that of Figure 22.

### 3.5 Ground Shield Offset

When the modulated data are binned in azimuth, a periodic signal due to the 12 panels of the ground shield is evident, especially on larger angular scales. The signal of period  $30^\circ$  is fit for an amplitude and is subtracted. Removal of the ground shield offset has less than 4% effect on the final angular power spectrum in all modulations, because when the data are binned in RA, the effect averages out.

The ground shield offset is computed from all fields and files in an observing set. A different ground shield offset is fit and removed for each channel,

modulation, and set. Figure 24 shows the azimuthally binned data for one set, the fit to the ground shield synchronous signal, and the same data with the ground shield offset removed. The ground shield offset is larger for data taken when the telescope is pointed closer to the ground shield and for modulations which probe larger angular scales, as illustrated in Figure 25.

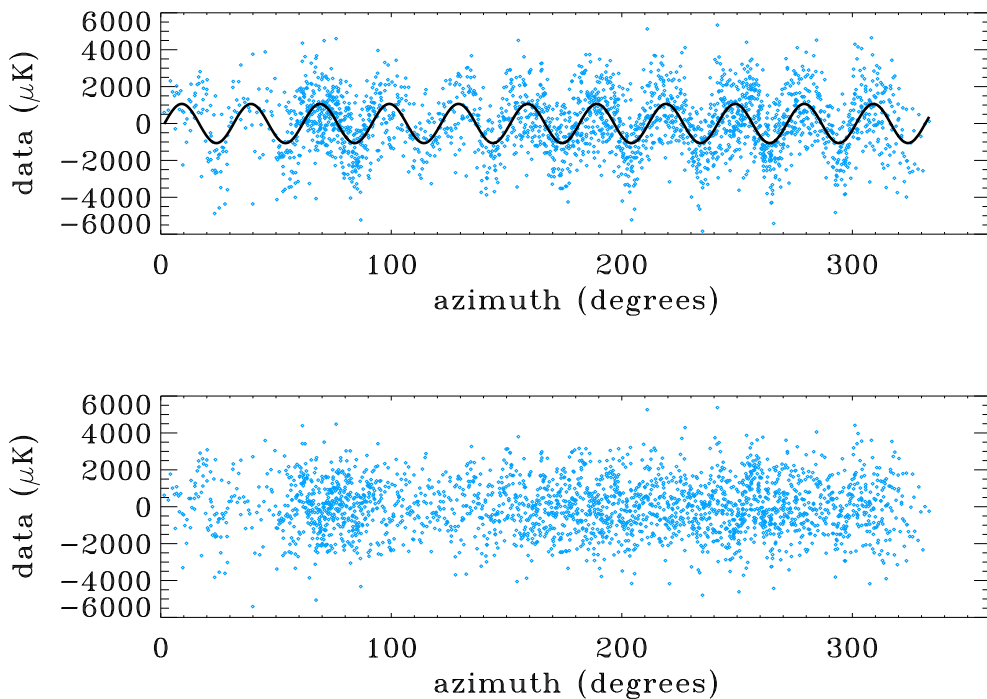


Figure 24 Top– Azimuthally binned data for channel 1, left-going chopper data, modulation 1, set j**9**. There are 2421 data points ( $269 \text{ files} \times 9 \text{ fields}$ ) plotted. The periodic signal caused by the 12 panels of the ground shield is evident and the best fit curve is plotted as a solid line. Bottom– the same data with the ground shield offset subtracted.

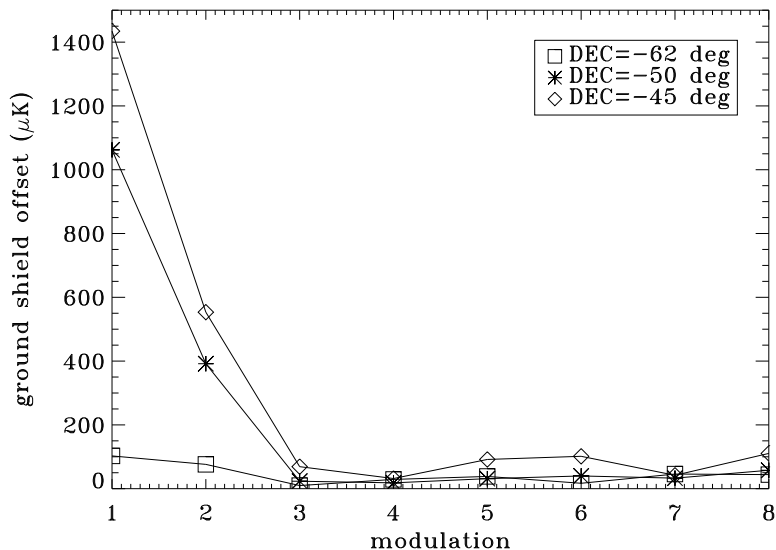


Figure 25 Amplitude of the ground shield offset as a function of declination and modulation for channel 1, left-going chopper cycles, file sets sb, jb, and nb. The offset is larger for data taken at a lower elevation, i.e. when the telescope is pointed closer to the ground shield.

### 3.6 Co-adding

After the data have been modulated and offsets removed, the right and left-going data, which have been properly phased, are co-added, as are data from channels which observe the same points on the sky. The bandpasses are similar enough in frequency range that the data can be co-added without loss of information. Hereafter channel 12 will refer to the co-added channel 1 and 2 data and channel 45 will refer to the co-added channel 4 and 5 data. Since the two feeds observe different points on the sky they cannot be



co-added; the theoretical and noise covariances between them are included in the likelihood analysis of the angular power spectrum.

### **3.7 60 Hz**

The South Pole Station power nominally operates at a frequency of 60 Hz, so there is possible contamination at 60 Hz and its harmonics. However, the chopper runs at 5.1 Hz, which is incommensurate with 60 Hz. To verify that a 60 Hz signal would not contaminate the data, we created a 60 Hz signal for one stare of data, modulated it, averaged over 164 cycles and found that the resulting signal is negligible for all modulations.

# CHAPTER 4

## DATA ANALYSIS TECHNIQUES

### 4.1 Bayesian Likelihood Analysis

In order to estimate parameters from data, a Bayesian likelihood analysis (see for example Readhead et al. 1989) is used. What we want to report from any experiment is the probability of the theory being true given the data,  $P(\text{theory}|\text{data})$ . What we can actually measure is the likelihood,  $\mathcal{L} = P(\text{data}|\text{theory})$ . Applying Bayes' theorem,

$$P(\text{theory}|\text{data}) \propto P(\text{data}|\text{theory})P(\text{theory}). \quad (4.1)$$

The prior probability,  $P(\text{theory})$ , is conservatively taken to be uniform (uninformative). This technique assumes the data are drawn from a Gaussian distribution on the sky.

The likelihood ( $\mathcal{L}$ ) can be written:

$$\mathcal{L} = (2\pi)^{-N/2} \det(\mathbf{C})^{-1/2} \exp(-\chi^2/2) \quad (4.2)$$

where  $\chi^2 = \vec{d}^t \mathbf{C}^{-1} \vec{d}$ ,  $\mathbf{C} = \mathbf{C}^T + \mathbf{C}^N + \mathbf{C}^C$ ,  $\vec{d}$  is the data,  $\mathbf{C}^T$  is the theory covariance matrix,  $\mathbf{C}^N$  is the noise covariance matrix, and  $\mathbf{C}^C$  is the constraint matrix for offset subtraction.  $\mathbf{C}^C$  for PyV is discussed in section 4.4 and  $\mathbf{C}^N$  for PyV is discussed in sections 5.2 and 6.1.

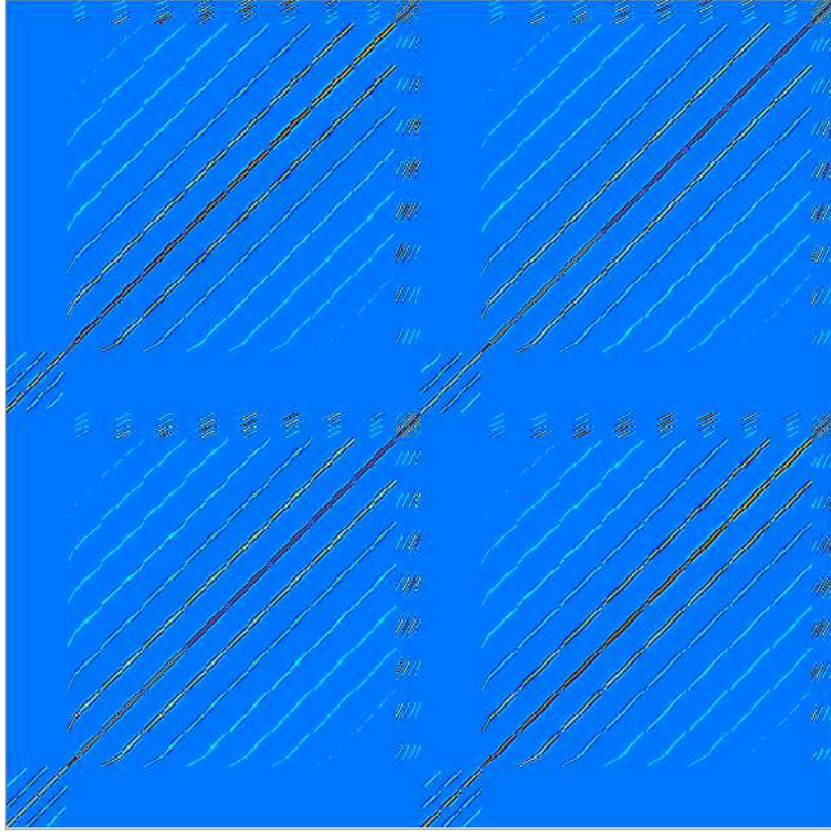


Figure 26 Theory covariance matrix,  $\mathbf{C}^T$ , for PyV modulation 2.  $C^T(1,1)$  is in the bottom left. The matrix is 690 x 690 for the 345 fields and 2 channels in the reduced, co-added data. Points 1:345 correspond to channel 45 and points 346:690 correspond to channel 12. There are significant theory correlations between channels because they are separated by  $2.80^\circ$  on the sky.

The theory covariance matrix,  $\mathbf{C}^T$ , depends on the model CMB angular power spectrum  $C_l$  and the experimental window functions  $W_{lij}$ . The elements of  $\mathbf{C}^T$  are given by

$$C_{ij}^T = \sum_l \frac{(2l+1)}{4\pi} C_l W_{lij}. \quad (4.3)$$

A sample theory covariance matrix is shown in Figure 26.

## 4.2 Window Functions

The window functions are a measure of experimental sensitivity as a function of angular scale  $l$ . They are generated from the experimental beam map, modulations, and observing strategy.

### 4.2.1 A Method For Calculating Window Functions

The following is a method for calculating the window functions for a general beam map and observing strategy in the flat sky approximation. Section 4.2.3 discusses the importance of using the exact beam map and observing strategy for certain experiments. The flat sky approximation is valid for many current and past CMB experiments. Another discussion of window functions can be found in White and Srednicki (1995). Figure 27 illustrates the geometry of the beam map and observing strategy used in the derivation below.

- The (modulated) beam map is  $B$ , which is 2-dimensional.  $B_m(\vec{x} - \vec{x}_i)$  is the beam map for modulation  $m$  corresponding to an observation at pixel  $i$ .
- $\theta_i$  is the twist of the beam map for pixel  $i$  with respect to the  $s_1$ -axis in Figure 27.

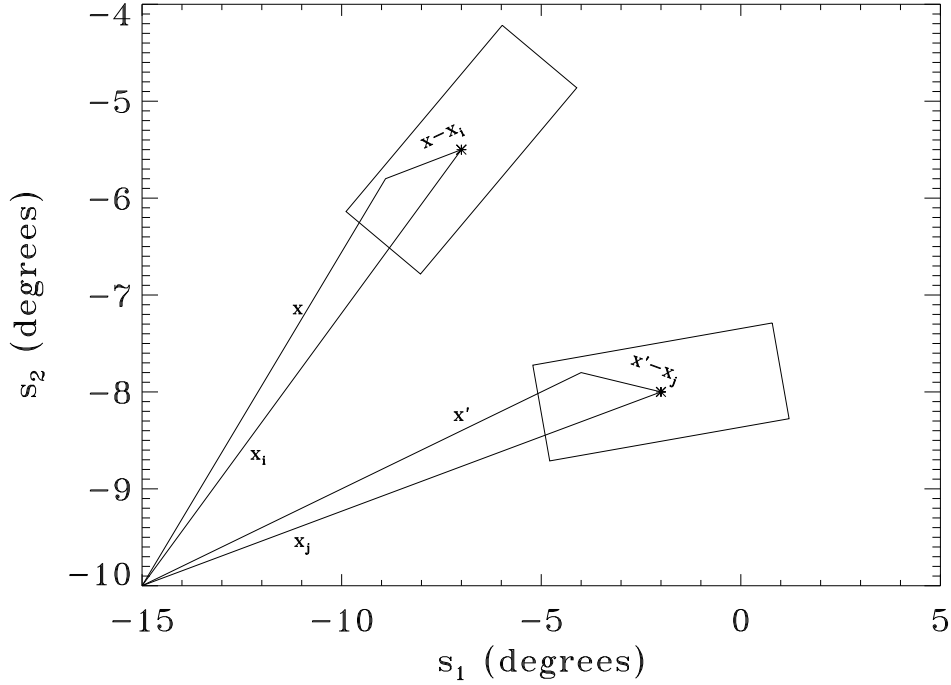


Figure 27 Position of beam maps for computing  $W_{lij}$ .  $s_1$  and  $s_2$  are flat space coordinates.

- The rotation matrix acting on  $(\vec{x} - \vec{x}_i)$  is  $\mathbf{R}_i = \begin{pmatrix} \cos(\theta_i) & -\sin(\theta_i) \\ \sin(\theta_i) & \cos(\theta_i) \end{pmatrix}$ .
- The measured anisotropy at a point is a convolution of the true anisotropy with the beam map:  $\Delta T_i = \int B_m(\mathbf{R}_i(\vec{x} - \vec{x}_i)) \Delta T(\vec{x}) d\vec{x}$ .
- The underlying temperature field  $\Delta T(\vec{x})$  can be expanded in spherical harmonics:  $\Delta T(\vec{x}) = \sum_{lm} a_{lm} Y_{lm}(\theta, \phi)$ , and the multipole moments,  $C_l$ , are  $C_l = \langle |a_{lm}|^2 \rangle$ .
- The elements of the theory covariance matrix are  $C_{ij}^T = \langle \Delta T_i \Delta T_j \rangle$ .

Using the above definitions, the elements of the theory covariance matrix are:

$$C_{ij}^T = \int \int B_m(\mathbf{R}_i(\vec{x} - \vec{x}_i)) B_{m'}(\mathbf{R}_j(\vec{x}' - \vec{x}_j)) \langle \Delta T(\vec{x}) \Delta T(\vec{x}') \rangle d\vec{x} d\vec{x}'. \quad (4.4)$$

Assuming rotational symmetry and averaging over the whole sky,

$$\langle \Delta T(\vec{x}) \Delta T(\vec{x}') \rangle = \sum \frac{(2l+1)}{4\pi} C_l P_l(\cos(q)), \quad (4.5)$$

where  $P_l$  are the Legendre polynomials associated with the spherical harmonic expansion,  $q = |\vec{q}|$ , and

$$\vec{q} = \vec{x} - \vec{x}'. \quad (4.6)$$

Defining dummy variables,

$$\begin{aligned} \vec{y} &= \mathbf{R}_i(\vec{x} - \vec{x}_i) \\ \vec{y}' &= \mathbf{R}_j(\vec{x}' - \vec{x}_j), \end{aligned} \quad (4.7)$$

we have

$$\begin{aligned} \vec{x} &= \mathbf{R}_i^{-1}(\vec{y}) + \vec{x}_i \\ \vec{x}' &= \mathbf{R}_j^{-1}(\vec{y}') + \vec{x}_j \\ d\vec{x} &= \mathbf{R}_i^{-1}(d\vec{y}) \\ d\vec{x}' &= \mathbf{R}_j^{-1}(d\vec{y}') \end{aligned} \quad (4.8)$$

Substituting these into equation 4.4, we have

$$C_{ij}^T = \int \int B_m(\vec{y}) B_{m'}(\vec{y}') \sum \frac{(2l+1)}{4\pi} C_l P_l(\cos(q)) \mathbf{R}_i^{-1}(d\vec{y}) \mathbf{R}_j^{-1}(d\vec{y}') \quad (4.9)$$

Defining the window functions  $W_{lij}$  by

$$C_{ij}^T = \sum_l \frac{(2l+1)}{4\pi} C_l W_{lij} \quad (4.10)$$

and combining equations 4.9 and 4.10, we get an expression for the window functions:

$$W_{lij} = \int \int B_m(\vec{y}) B_{m'}(\vec{y}') P_l(\cos q) \mathbf{R}_i^{-1}(d\vec{y}) \mathbf{R}_j^{-1}(d\vec{y}'). \quad (4.11)$$

This is a four-dimensional integral, which is computationally intensive. In order to reduce the dimensionality of the integral to be able calculate the window functions in a reasonable amount of time on a workstation, we make the flat sky approximation that for large  $l$ ,

$$P_l(\cos q) = J_0(lq). \quad (4.12)$$

The expression for the window functions then becomes

$$W_{lij} = \int \int B_m(\vec{y}) B_{m'}(\vec{y}') J_0(lq) \mathbf{R}_i^{-1}(d\vec{y}) \mathbf{R}_j^{-1}(d\vec{y}'). \quad (4.13)$$

Using the identity

$$J_0(lq) = (1/2\pi) \int d\phi e^{-ilq\cos\phi}, \quad (4.14)$$

and substituting into equation 4.13, we have

$$W_{lij} = (1/2\pi) \int \int \int B_m(\vec{y}) B_{m'}(\vec{y}') e^{-ilq\cos\phi} d\phi \mathbf{R}_i^{-1}(d\vec{y}) \mathbf{R}_j^{-1}(d\vec{y}'). \quad (4.15)$$

Defining a vector  $\vec{k}$  such that  $|\vec{k}| = l$  and  $\vec{k} \cdot \vec{q} = lq\cos\phi$ , equation 4.15 becomes

$$W_{kij} = (1/2\pi) \int \int \int B_m(\vec{y}) B_{m'}(\vec{y}') e^{-i\vec{k} \cdot \vec{q}} d\phi \mathbf{R}_i^{-1}(d\vec{y}) \mathbf{R}_j^{-1}(d\vec{y}'). \quad (4.16)$$

From equations 4.6 and 4.8, we have

$$\vec{q} = \mathbf{R}_i^{-1}(\vec{y}) + \vec{x}_i - \mathbf{R}_j^{-1}(\vec{y}') - \vec{x}_j. \quad (4.17)$$

Substituting equation 4.17 into equation 4.16, the window functions become

$$W_{kij} = (1/2\pi) \int \int \int B_m(\vec{y}) B_{m'}(\vec{y}') e^{-i\vec{k} \cdot (\mathbf{R}_i^{-1}(\vec{y}) + \vec{x}_i - \mathbf{R}_j^{-1}(\vec{y}') - \vec{x}_j)} d\phi \mathbf{R}_i^{-1}(d\vec{y}) \mathbf{R}_j^{-1}(d\vec{y}'). \quad (4.18)$$

Since we are integrating over all  $\vec{y}$  and since the determinant of the rotation matrix is 1, we can write this as

$$W_{kij} = (1/2\pi) \int \int \int B_m(\vec{y}) B_{m'}(\vec{y}') e^{-i\vec{k} \cdot (\mathbf{R}_i^{-1}(\vec{y}) + \vec{x}_i - \mathbf{R}_j^{-1}(\vec{y}') - \vec{x}_j)} d\phi d\vec{y} d\vec{y}'. \quad (4.19)$$

Rearranging a few terms,

$$W_{kij} = (1/2\pi) \int e^{-i\vec{k} \cdot (\vec{x}_i - \vec{x}_j)} d\phi \int e^{-i\vec{k} \cdot (\mathbf{R}_i^{-1}(\vec{y}))} B_m(\vec{y}) d\vec{y} \int e^{+i\vec{k} \cdot \mathbf{R}_j^{-1}(\vec{y}')} B_{m'}(\vec{y}') d\vec{y}'. \quad (4.20)$$

Equation 4.20 can be written in terms of the Fourier transformed beam maps, yielding the final expression for the window functions:

$$W_{kij} = (1/2\pi) \int e^{-i\vec{k} \cdot (\vec{x}_i - \vec{x}_j)} \tilde{B}_m(\vec{k} \mathbf{R}_i^{-1}) \tilde{B}_{m'}^*(\vec{k} \mathbf{R}_j^{-1}) d\phi. \quad (4.21)$$

The four-dimensional integral of equation 4.11 has been reduced to a one-dimensional integral and a Fourier transform, saving computing time. The window functions can be saved to disk for quick computation of  $\mathbf{C}^T$  for various input  $C_l$  spectra using equation 4.10.



We will refer to the array  $W_{lij}$  as the window functions and to  $W_l = W_{lii}$  as the diagonal window functions.

#### *4.2.2 Normalization of the Beam Map*

The modulated beam map is created by convolving the (spatial) modulation pattern with the beam and is usually normalized by  $(1/2\pi\sigma^2)$ , where  $\sigma$  characterizes the width of a symmetric Gaussian beam, or  $\sigma = \sqrt{\frac{1}{2}(\sigma_x\sigma_y)}$  in the case of an asymmetric Gaussian. The normalization of the modulations usually follows the convention discussed in 3.2.

Some experiments do not follow this beam normalization. For example, for the MSAM-I experiment (Cheng et al. 1997), which does not have a Gaussian beam, the beam map and data are normalized consistently with each other, but the data are in units of  $\mu K deg^2$  rather than  $\mu K$ .

#### *4.2.3 Approximations*

Depending on the experiment, some approximations can affect the window functions. For example, for the MSAM-I experiment, a Gaussian beam is a poor approximation. Its impact on the window functions is shown in Figure 28. Ignoring the twist of the MSAM-I experiment is also a poor approximation, as shown in Figure 29.

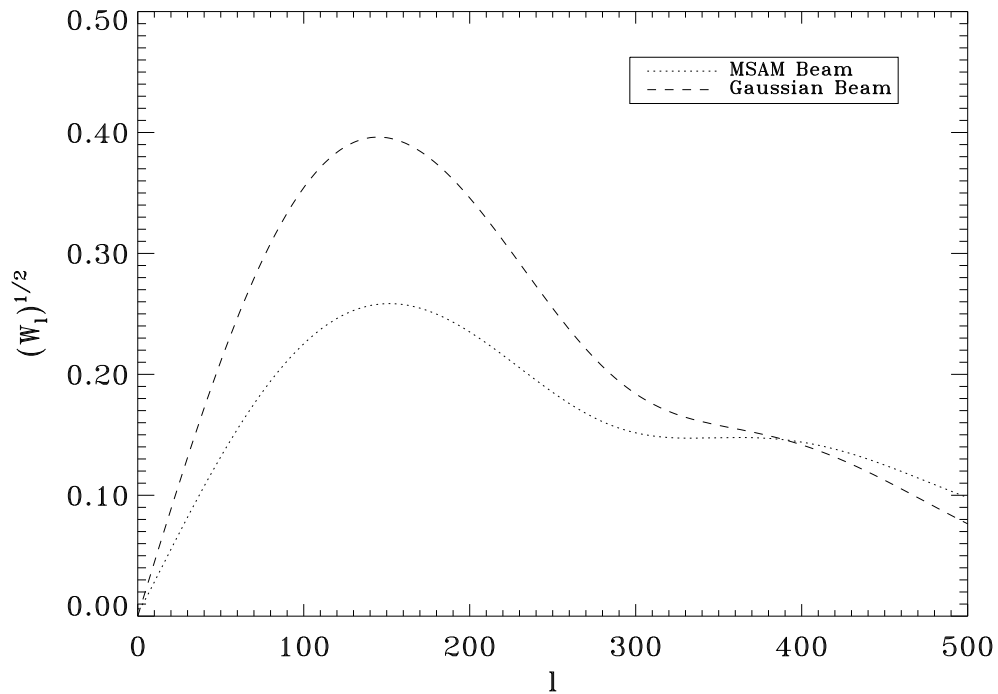


Figure 28 Diagonal window functions for MSAM-I with a Gaussian beam and with the true beam.

#### 4.2.4 Analytic Expressions

This section provides some concrete examples of window functions for observing strategies and beam maps which can be treated analytically. Examples will be given for 3 cases of analytic expressions: (1) calculation of the full window function array in the flat space approximation, (2) calculation of the diagonal window functions in the flat space approximation, and (3) calculation of the diagonal window functions without the flat space approximation.

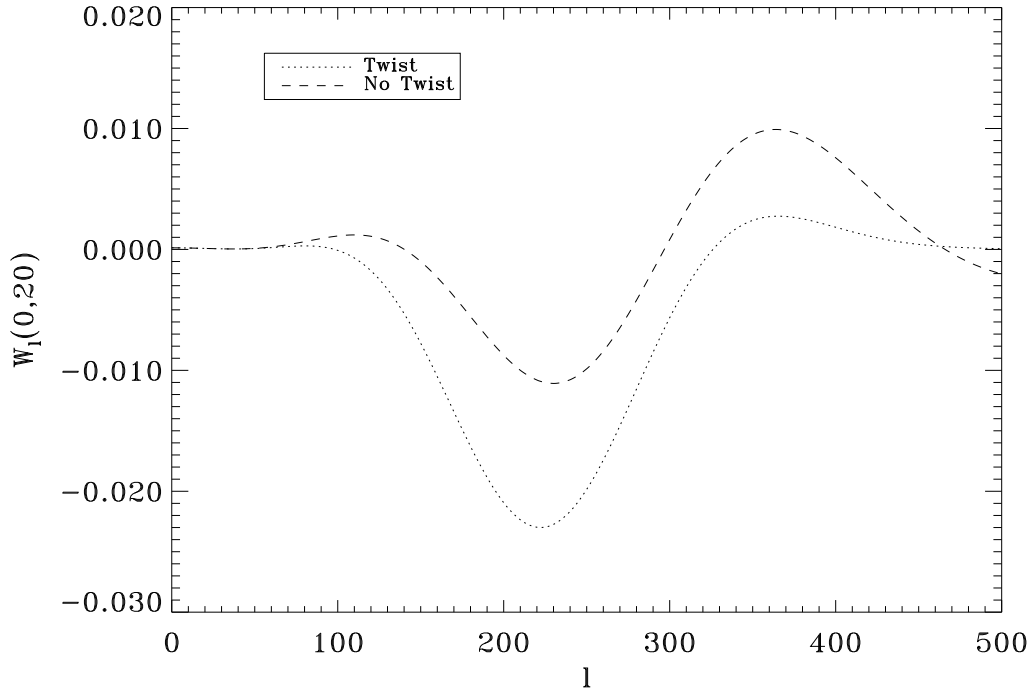


Figure 29 Effect of twist on the window functions. Including twist is important for the MSAM-I experiment.

- Case 1: Two examples of the full window function array given by equation 4.21 are given below.

Example 1.1. Gaussian beam.

The beam map for a symmetric Gaussian beam of width  $\sigma$  is given by

$$B(\vec{a}) = \frac{1}{2\pi\sigma^2} e^{-a^2/(2\sigma^2)}, \quad (4.22)$$

so the Fourier transform of the beam map is

$$\tilde{B}(k) = e^{-k^2\sigma^2/2}. \quad (4.23)$$

Using equation 4.21 the window functions are:

$$\begin{aligned} W_{kij} &= \frac{1}{2\pi} e^{-k^2\sigma^2} \int_0^{2\pi} d\theta e^{-ik|\vec{x}_i - \vec{x}_j| \cos(\theta)} \\ &= e^{-l^2\sigma^2} J_0(l|\vec{x}_i - \vec{x}_j|). \end{aligned} \quad (4.24)$$

Example 1.2. Single difference Gaussian beam.

The beam map for a symmetric Gaussian beam modulated with a single difference chop is given by

$$B(\vec{a}) = \frac{1}{2\pi\sigma^2} [e^{-|\vec{a} - \vec{a}_0|^2/(2\sigma^2)} - e^{-|\vec{a} + \vec{a}_0|^2/(2\sigma^2)}] \quad (4.25)$$

and its Fourier transform is

$$\tilde{B}(\vec{k}) = e^{-k^2\sigma^2/2} [e^{-i\vec{k}\cdot\vec{a}_0} - e^{+i\vec{k}\cdot\vec{a}_0}]. \quad (4.26)$$

Using equation 4.21, the window functions are

$$W_{kij} = \frac{1}{2\pi} e^{-k^2\sigma^2} \int_0^{2\pi} d\theta e^{-i\vec{k}\cdot(\vec{x}_i - \vec{x}_j)} [e^{-i\vec{k}_i\cdot\vec{a}_0} - e^{+i\vec{k}_i\cdot\vec{a}_0}] [e^{+i\vec{k}_j\cdot\vec{a}_0} - e^{-i\vec{k}_j\cdot\vec{a}_0}] \quad (4.27)$$

where  $\vec{k}_i = \vec{k}\mathbf{R}_i^{-1}$ . Simplifying using equation 4.14, we have

$$\begin{aligned} W_{lij} &= e^{-l^2\sigma^2} [J_0(l|\vec{x}_i - \vec{x}_j + \vec{a}_{0i} - \vec{a}_{0j}|) \\ &\quad + J_0(l|\vec{x}_i - \vec{x}_j - \vec{a}_{0i} + \vec{a}_{0j}|) \\ &\quad - J_0(l|\vec{x}_i - \vec{x}_j - \vec{a}_{0i} - \vec{a}_{0j}|) \\ &\quad - J_0(l|\vec{x}_i - \vec{x}_j + \vec{a}_{0i} + \vec{a}_{0j}|)] \end{aligned} \quad (4.28)$$

where  $\vec{a}_{0i} = \mathbf{R}_i^{-1}\vec{a}_0$ .

• Case2: For just the diagonal window functions, equation 4.21 simplifies to

$$W_{kii} = (1/2\pi) \int d\phi |\tilde{B}_m(\vec{k})|^2. \quad (4.29)$$

The following are examples of equation 4.29 for simple beams and chopping strategies.

Example 2.1. Single difference Gaussian beam.

The diagonal window functions are:

$$W_l = \tilde{B}_g^2(l)2[1 - J_0(2l\theta_c)] \quad (4.30)$$

where

$$\tilde{B}_g(l) = e^{-l^2\sigma^2/2} \quad (4.31)$$

is the Fourier transform of an (unmodulated) symmetric Gaussian beam.

Example 2.2. Double difference Gaussian beam.

The diagonal window functions are:

$$W_l = \tilde{B}_g^2(l)\left[\frac{3}{2} - 2J_0(l\theta_c) + \frac{1}{2}J_0(2l\theta_c)\right] \quad (4.32)$$

Example 2.3. Single difference top hat beam.

The diagonal window functions are:

$$W_l = \tilde{B}_t^2(l)2[1 - J_0(2l\theta_c)] \quad (4.33)$$

where

$$\tilde{B}_t(l) = [2J_1(l\theta_t)]/(l\theta_t) \quad (4.34)$$

is the Fourier transform of a top hat beam of characteristic size  $\theta_t$ .

Example 2.4. Double difference top hat beam.

The diagonal window functions are:

$$W_l = \tilde{B}_l^2(l) \left[ \frac{3}{2} - 2J_0(l\theta_c) + \frac{1}{2}J_0(2l\theta_c) \right] \quad (4.35)$$

• Case 3: The diagonal window functions for a general modulation pattern, without assuming the flat sky approximation are given by

$$W_{lmm'} = \tilde{B}^2(l) \sum_s \sum_{s'} M_{ms} M_{m's'} P_l(\cos(\theta_s - \theta_{s'})) \quad (4.36)$$

where  $\theta$  is the chopper angle as a function of sample  $s$  and  $M_m$  is the amplitude of modulation  $m$ .  $\tilde{B}^2(l)$  is the spherical transform of the (unmodulated) beam map. The beam must be symmetric. Some examples of equation 4.36 are given below.

Example 3.1. Single difference Gaussian beam.

The modulation is given by:

$$M = \begin{cases} +1 & \text{at } \theta = -\theta_c \quad (s = 1) \\ -1 & \text{at } \theta = +\theta_c \quad (s = 2). \end{cases} \quad (4.37)$$

and the spherical transform of a Gaussian beam is given by

$$\tilde{B}(l) = e^{-\frac{1}{2}l(l+1)\sigma^2}. \quad (4.38)$$

Thus, from equation 4.36, the diagonal window functions are

$$\begin{aligned}
W_l &= \tilde{B}_g^2(l) \sum_{s=1}^2 \sum_{s'=1}^2 M_{ms} M_{m's'} P_l(\cos(\theta_s - \theta_{s'})) \\
&= \tilde{B}_g^2(l) [(+1)(+1)P_l(\cos(-\theta_c + \theta_c)) \\
&\quad + (+1)(-1)P_l(\cos(-\theta_c - \theta_c)) \\
&\quad + (-1)(+1)P_l(\cos(+\theta_c + \theta_c)) \\
&\quad + (-1)(-1)P_l(\cos(+\theta_c - \theta_c))] \\
&= \tilde{B}_g^2(l) [P_l(\cos(0)) - P_l(\cos(-2\theta_c)) \\
&\quad - P_l(\cos(2\theta_c)) + P_l(\cos(0))]
\end{aligned} \tag{4.39}$$

$$W_l = \tilde{B}_g^2(l) 2[1 - P_l(\cos 2\theta_c)] \tag{4.40}$$

Example 3.2. Double difference Gaussian beam.

The modulation is given by

$$M = \begin{cases} -1/2 & \text{at } \theta = -\theta_c & (s = 1) \\ +1 & \text{at } \theta = 0 & (s = 2) \\ -1/2 & \text{at } \theta = +\theta_c & (s = 3) \end{cases} \tag{4.41}$$

and the diagonal window functions are given by

$$W_l = \tilde{B}_g^2(l) \left[ \frac{3}{2} - 2P_l(\cos\theta_c) + \frac{1}{2}P_l(\cos 2\theta_c) \right]. \tag{4.42}$$

Example 3.3. Four-point-chop Gaussian beam.

The modulation is given by

$$M = \begin{cases} -1/4 & \text{at } \theta = -\frac{3}{2}\theta_c & (s = 1) \\ +3/4 & \text{at } \theta = -\frac{1}{2}\theta_c & (s = 2) \\ -3/4 & \text{at } \theta = +\frac{1}{2}\theta_c & (s = 3) \\ +1/4 & \text{at } \theta = +\frac{3}{2}\theta_c & (s = 4) \end{cases} \quad (4.43)$$

and the diagonal window functions are given by

$$W_l = \tilde{B}_g^2(l) \left[ \frac{5}{4} - \frac{15}{8} P_l(\cos \frac{2}{3}\theta_c) + \frac{3}{4} P_l(\cos \frac{4}{3}\theta_c) - \frac{1}{8} P_l(\cos 2\theta_c) \right]. \quad (4.44)$$

A summary of the diagonal window functions for simple chopping strategies is given in Table 6. The diagonal window functions in the flat space approximation are similar to the ones calculated not assuming the flat space approximation except that the Legendre polynomials  $P_l(\cos\theta_c)$  are replaced by Bessel functions  $J_0(l\theta_c)$ . Figure 30 shows the diagonal window functions for single and double difference Gaussians with and without the flat space approximation.

modulation	$W_l$
2-point	$2[1 - P_l(\cos 2\theta_c)]$
3-point	$[\frac{3}{2} - 2P_l(\cos\theta_c) + \frac{1}{2}P_l(\cos 2\theta_c)]$
4-point	$[\frac{5}{4} - \frac{15}{8}P_l(\cos \frac{2}{3}\theta_c) + \frac{3}{4}P_l(\cos \frac{4}{3}\theta_c) - \frac{1}{8}P_l(\cos 2\theta_c)]$

Table 6 Summary of analytic expressions for diagonal window functions for simple chopping strategies. All are multiplied by  $\tilde{B}^2(l)$ . The flat space approximations are the same except the Legendre polynomials  $P_l(\cos\theta_c)$  are replaced by Bessel functions  $J_0(l\theta_c)$ .



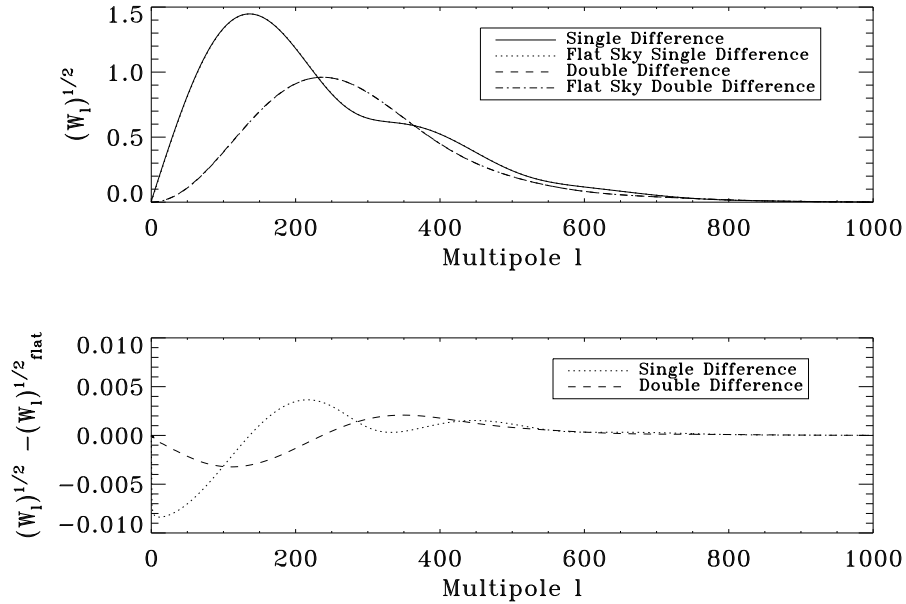


Figure 30 Diagonal window functions with and without the flat sky approximation. Shown in the top panel are  $W_l^{1/2}$  for single and double difference chops of  $\theta_c = 0.7^\circ$  and a Gaussian beam of width  $\sigma = 0.212^\circ$ . Shown in the bottom panel are the residuals.

#### 4.2.5 Python V Window Functions

For the PyV observing strategy, equation 4.21 becomes

$$W_{lij} = (1/2\pi) \int e^{-i\vec{k}\cdot(\vec{x}_i - \vec{x}_j)} \tilde{B}(\vec{k}) \tilde{B}^*(\vec{k}) d\phi \quad (4.45)$$

where  $\tilde{B}(\vec{k})$  is the Fourier transform of the beam map for the given modulation,  $\vec{x}_i$  the position of field  $i$ , and  $\vec{k} = l(\cos \phi, \sin \phi)$ . These functions are computed for all pairs of fields and channels. Figure 31 shows the PyV diagonal window functions. A different modulated beam map is used at each declination because the total chopper throw, which is constant in azimuth

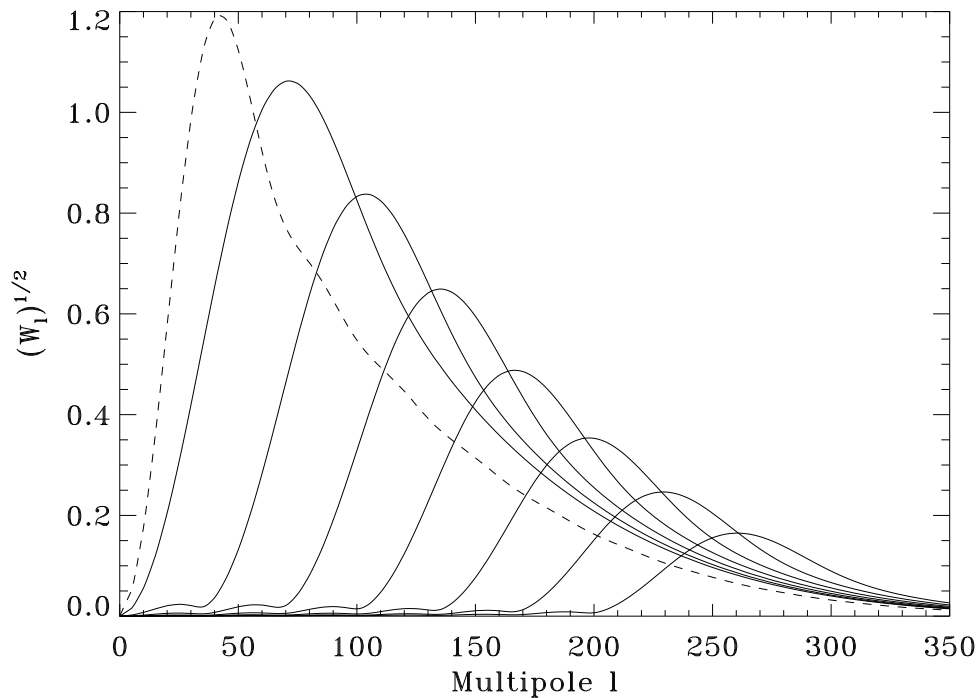


Figure 31 Diagonal window functions for PyV at a declination of  $-49^\circ$ . The unapodized cosine modulation is plotted with a dashed line and the apodized cosine modulations are plotted with solid lines.

degrees, subtends fewer real degrees on the sky at higher declinations.

### 4.3 KL Decomposition

Karhunen-Loeve (KL) decomposition (see for example Tegmark et al. 1996), also known as the signal-to-noise eigenmode method (Bond 1994), transforms the data into a basis in which modes of the data can be sorted by their signal-to-noise (S/N).

This technique is useful for testing the self-consistency of data sets, for examining modes with a particular S/N range, and for data compression.

Calculation of the determinant in equation 4.2 is an  $N^3$  process and calculation  $\mathbf{C}^{-1}\vec{d}$  is an  $N^2$  process (see for example the backslash command in MATLAB), where  $N$  is the number of data points. By eliminating the modes which do not contribute to parameter estimation, (i.e. the ones with low S/N), KL decomposition can compress data sets with a minimal loss of information, speeding up the data analysis process typically by 3 orders of magnitude.

The steps for KL decomposition are as follows:

1. Let  $\mathbf{C}^{\mathbf{N}'} = \mathbf{C}^{\mathbf{N}} + \mathbf{C}^{\mathbf{C}}$ .
2. Calculate  $(\mathbf{C}^{\mathbf{N}'})^{-1/2}$ , for example by Cholesky decomposition.
3. Calculate the matrix

$$\mathbf{M} = (\mathbf{C}^{\mathbf{N}'})^{-1/2} \mathbf{C}^{\mathbf{T}} (\mathbf{C}^{\mathbf{N}'})^{-t/2}. \quad (4.46)$$

4. Calculate  $\mathbf{R}$ , the matrix of eigenvectors of  $\mathbf{M}$ .
5. Sort  $\mathbf{R}$  by eigenvalue. The eigenvalues are a measure of signal/noise.
6. The compression matrix  $\mathbf{B}'$  is the first  $N_{\text{keep}}$  rows of  $\mathbf{B} = \mathbf{R}(\mathbf{C}^{\mathbf{N}'})^{-1/2}$ , where  $N_{\text{keep}}$  is the number of KL modes to keep.

7. Then the theory matrix in the KL basis is

$$\mathbf{C}_{\text{KL}}^{\text{T}} = (\mathbf{B}')\mathbf{C}^{\text{T}}(\mathbf{B}')^t, \quad (4.47)$$

the data in the KL basis is

$$\vec{d}_{\text{KL}} = (\mathbf{B}')\vec{d}, \quad (4.48)$$

and the noise matrix in the KL basis is the identity matrix  $I$ .

#### 4.4 Constraint Matrices For Offsets

The subtraction of offsets can be accounted for as an additional term in the covariance matrix (e.g., Bond et al. 1998). For PyV, we must take into account the subtraction of the chopper synchronous offset and the ground shield synchronous offset.

In both cases, the subtracted data in field  $i$  is given by:

$$\begin{aligned} \hat{d}^i &= \frac{1}{N_{\text{files}}} \sum_{n=1}^{N_{\text{files}}} (d_n^i - \kappa f_n^i) \\ &\equiv \bar{d}^i - \kappa \bar{f}^i \end{aligned} \quad (4.49)$$

where  $\bar{f}^i$  is the mean of the offset vector which has been subtracted from field  $i$ . Both constraint matrices thus have the form

$$C_{ij}^C = \kappa \langle \bar{f}_i \bar{f}_j \rangle. \quad (4.50)$$

The chopper synchronous offset is constant over a file and the same chopper offset has been subtracted from fields  $i$  and  $j$ , thus  $\bar{f}^i = \bar{f}^j$  and the constraint matrix takes the form:

$$\mathbf{C}^{\text{CH}} = (\kappa_1/N_{\text{files}}) \quad (4.51)$$

for fields taken with the same set of files and zero for fields not taken with the same set of files.  $N_{\text{files}}$  is the number of files which observed the fields. Even if the offset subtracted is not perfectly estimated, taking  $\kappa_1$  to be large ensures that we have no sensitivity to modes of the data that could have come from the chopper. An image of the chopper constraint matrix is shown in Figure 32.

In the case of the ground shield synchronous offset,  $\bar{f}^i \neq \bar{f}^j$ . The ground shield constraint matrix is:

$$C_{ij}^{\text{GS}} = \kappa_2 \langle \bar{f}_i \bar{f}_j \rangle. \quad (4.52)$$

for fields  $i$  and  $j$  taken with the same set of files, and is zero for fields not taken with the same set of files. For each field  $i$ ,  $\bar{f}_i$  is known from the data reduction process (section 3.5). There is a different ground shield constraint matrix for each modulation. Again,  $\kappa_2$  is taken to be large. An image of the ground shield constraint matrix is shown in Figure 33.

We will refer to the total constraint matrix for PyV as  $\mathbf{C}^{\text{C}} = \mathbf{C}^{\text{CH}} + \mathbf{C}^{\text{GS}}$ .

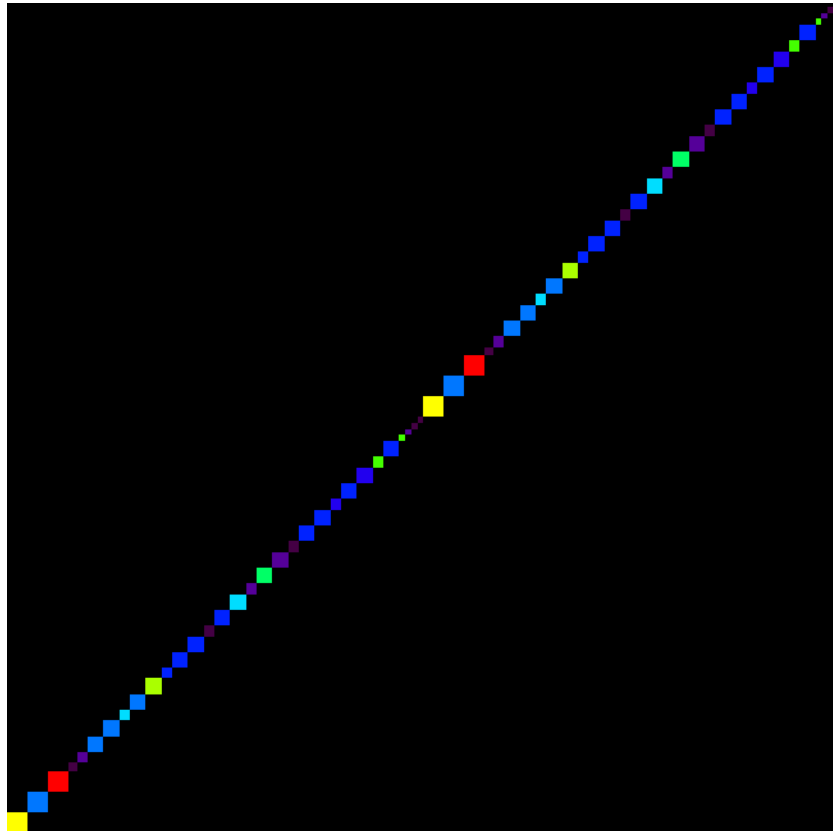


Figure 32 Image of chopper offset constraint matrix.  $C^{CH}(1,1)$  is in the bottom left corner of the image. The matrix is 690 x 690 for the 345 fields and 2 channels in the reduced, co-added data. Points 1:345 correspond to channel 45 and points 346:690 correspond to channel 12.

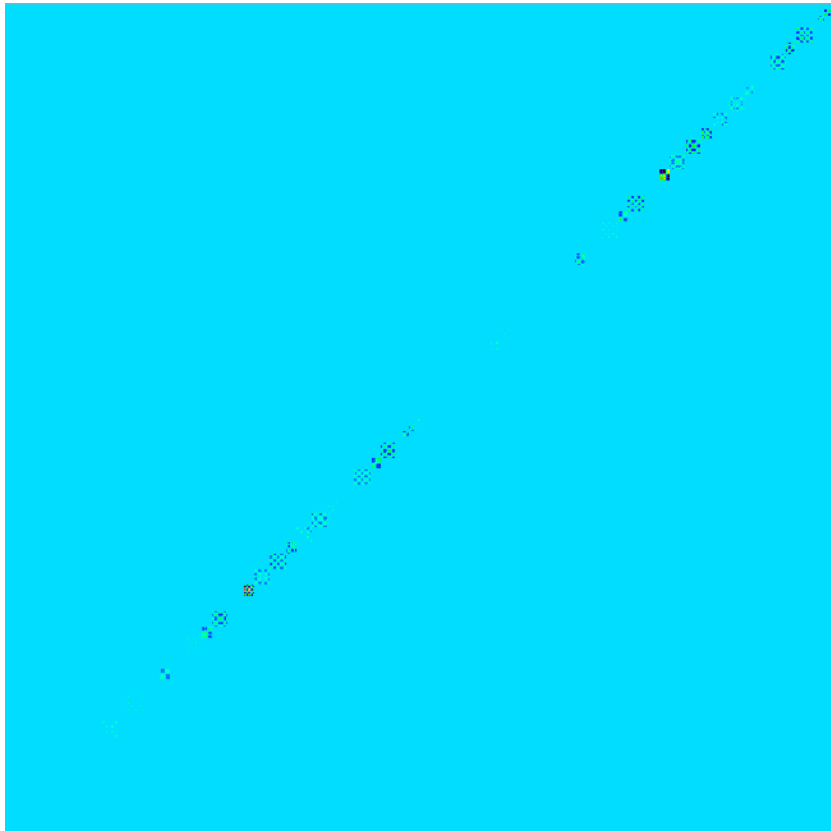


Figure 33 Image of ground shield constraint matrix for modulation 2.  $C^{GS}(1,1)$  is in the bottom left corner of the image. The matrix is 690 x 690 for the 345 fields and 2 channels in the reduced, co-added data. Points 1:345 correspond to channel 45 and points 346:690 correspond to channel 12.

## CHAPTER 5

### SINGLE MODULATION ANALYSIS

The angular power spectrum is first estimated from the PyV data set by considering each modulation separately. An analysis which includes cross-modulation correlations and which estimates the angular power spectrum simultaneously in a series of  $l$ -space bands is discussed in Chapter 6. This single modulation analysis is simpler computationally and conceptually than the cross-modulation analysis. The reduced PyV data set contains  $690 \text{ pixels} \times 8 \text{ modulations} = 5520 \text{ data points}$ . Computing the likelihood is considerably faster if 8  $690 \times 690$  matrices rather than a  $5520 \times 5520$  matrix is used. Additionally, the cross-modulation noise was difficult to model, as will be discussed in Chapter 6.

#### 5.1 Power Spectrum Constraints

A flat power spectrum is one for which  $\mathcal{C} \equiv (l(l+1)C_l/2\pi)$  is constant. For each of the eight modulations, we compute the likelihood ( $\mathcal{L}$ ) as a function of  $\mathcal{C} \equiv (l(l+1)C_l/2\pi)$  following equation 4.2. Limits are obtained from the likelihood curves following the prescription of Ganga et al. (1996), by



integrating  $\mathcal{L}$  over  $\mathcal{C}^{1/2}$  starting with the most likely value of  $\mathcal{C}^{1/2}$  and slicing at equal values of  $\mathcal{L}$  until 68% of the total area under the curve is reached for  $1\sigma$  limits or 95% of the total area under the curve is reached for  $2\sigma$  limits. An example likelihood curve and resulting limits are shown in Figure 34.

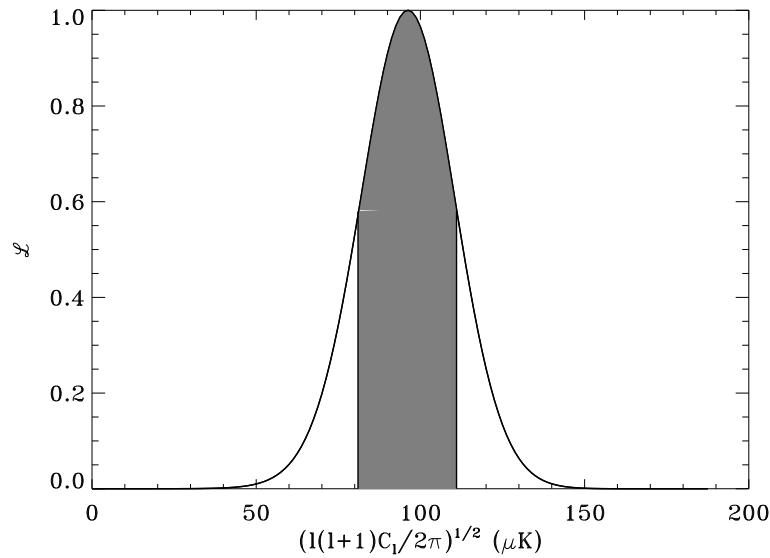


Figure 34 Getting limits from a likelihood curve. The likelihood curve and  $1\sigma$  limits for modulation 6 are shown as a typical example. The shaded area is 68% of the total area under the curve.

The CMB power spectrum is shown in Figure 35 and is given in Table 7. The band powers shown in Figure 35 are calculated for each modulation separately. The error bars include statistical uncertainties only and do not include uncertainties in the calibration or beam size. The calibration uncertainty allows all band powers to shift by the same amount (i.e. the calibration errors are correlated). Given the beam size uncertainty of approximately

mode	$l_e$	$(l(l+1)C_l/2\pi)^{1/2}$
1	$50^{+44}_{-29}$	$23^{+3}_{-3}$
2	$74^{+56}_{-39}$	$26^{+4}_{-4}$
3	$108^{+49}_{-41}$	$31^{+5}_{-4}$
4	$140^{+45}_{-41}$	$28^{+8}_{-9}$
5	$172^{+43}_{-40}$	$54^{+10}_{-11}$
6	$203^{+41}_{-39}$	$96^{+15}_{-15}$
7	$233^{+40}_{-38}$	$91^{+32}_{-38}$
8	$264^{+39}_{-37}$	$0^{+91}_{-0}$

Table 7 Angular power spectrum constraints from the single modulation likelihood analysis. Band powers are in  $\mu K$ .

$0.015^\circ$ , the band power for a given modulation can move roughly by a factor of  $\exp(\pm l(0.425)(0.015)(\pi/180))$ , only a 3% effect at  $l = 200$ . The effective  $l$  of each modulation is given by

$$l_e = \frac{I(lW_l)}{I(W_l)} \quad (5.1)$$

where

$$I(W_l) = \sum_l \frac{(l + \frac{1}{2})W_l}{l(l+1)}. \quad (5.2)$$

The  $l$  range of each modulation is determined by the half-maximum points of  $(W_l)^{1/2}$  and is indicated as horizontal error bars.

## 5.2 Noise Model

Our noise model assumes the covariance between fields taken with different sets of files is negligible because of the chopper offset removal and

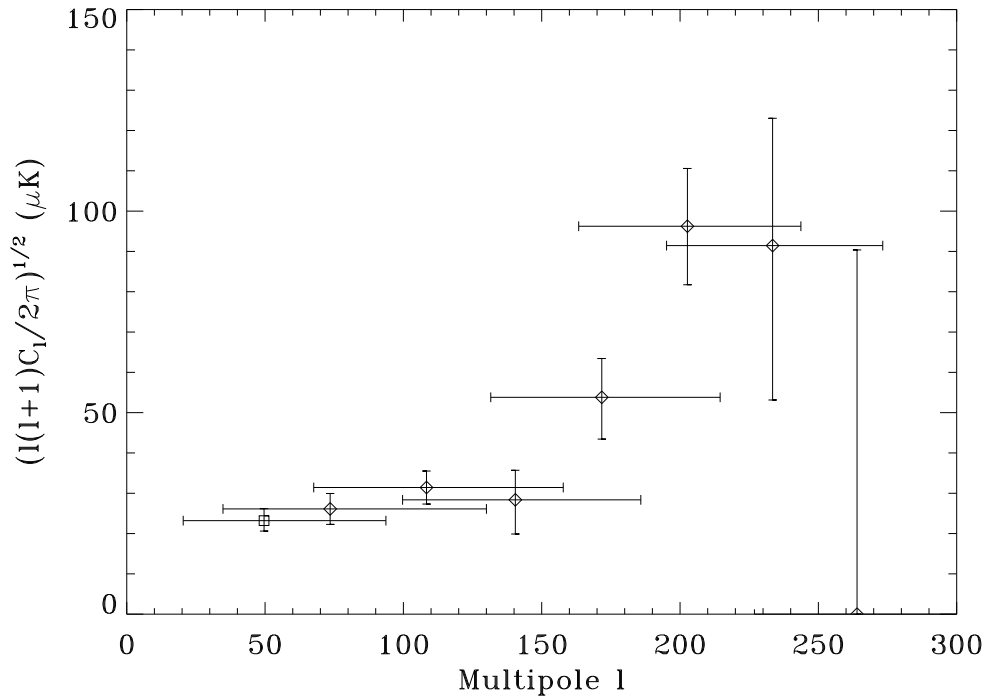


Figure 35 PyV angular power spectrum constraints from the single modulation analysis. The detections have  $1\sigma$  error bars and the upper limit has  $2\sigma$  error bars. The unapodized cosine modulation is plotted with an open square and the apodized cosine modulations are plotted with diamonds. The error bars include statistical uncertainties only and do not include uncertainties in the calibration or beam size. The  $l$  range of each modulation is determined by the half-maximum points of  $(W_l)^{1/2}$ . Low  $l$  values correspond to large angular scales and high  $l$  values correspond to small angular scales. CMB power is clearly rising from low to high  $l$  up to the sensitivity cutoff of PyV.

because of the long time (at least 10 hours) between measurements. An analysis comparing the noise covariance estimated from data which had not yet been co-added over all cycles and the noise covariance estimated from data which had been co-added over all cycles indicates that PyV noise is dominated by detector noise. However, the long term drifts due to the at-

mosphere, which add to the variance as well as induce small correlations between fields taken with the same set of files, could be important, especially for power spectrum estimation.

The noise covariance between fields taken with the same set of files is first estimated by taking the usual covariance on the co-added data:

$$N_{\text{files}} C_{ij}^N = \frac{1}{N_{\text{files}} - 1} \sum_{n=1}^{N_{\text{files}}} (d_n^i - \bar{d}^i)(d_n^j - \bar{d}^j) \quad (5.3)$$

where

$$\bar{d}^i = \frac{1}{N_{\text{files}}} \sum_{n=1}^{N_{\text{files}}} d_n^i, \quad (5.4)$$

$d^i$  is the data from field  $i$ ,  $d^j$  is the data from field  $j$  and  $N_{\text{files}}$  is the number of files in the set containing fields  $i$  and  $j$ . However, since there were typically only 100 files taken for each field, the sample variance on the noise estimate is  $\sim 1/(100)^{1/2}$ , or 10%, which will severely bias estimates of band power. To obtain a better estimate of the noise, we averaged the variances for each set of files and then scaled the off-diagonal elements of the covariance to the average variance in a given set based on a model derived from the entire PyV data set.

In order to derive a noise model for the single modulation analysis we examined histograms of  $\mathbf{C}^N N_{\text{files}}$  for each modulation as a function of stare lag from 0 to +16 for channels 12 and 45 and from -16 to +16 for the cross-covariance between channels 12 and 45. Examples are shown in Figures 36

and 37. We also examined plots of the mean of  $C^N N_{\text{files}}$  for each modulation as a function of stare lag. If the off-diagonal correlations were due entirely to the chopper offset subtraction and white noise, the noise matrix would be of the form:

$$C_{ij}^N N_{\text{files}} = \left( \delta_{ij} - \frac{1}{N_{\text{stares}}} \right) \sigma^2 \quad (5.5)$$

for fields  $i$  and  $j$  in the same observing set and noise variance  $\sigma^2$ . As illustrated in Figure 38  $C^N N_{\text{files}}$  is not flat as in equation 5.5, but has some taper, indicating that long term drifts, perhaps due to atmosphere, could be important. The cross-channel covariances are small but non-zero. A sample noise covariance matrix is shown in Figure 39.

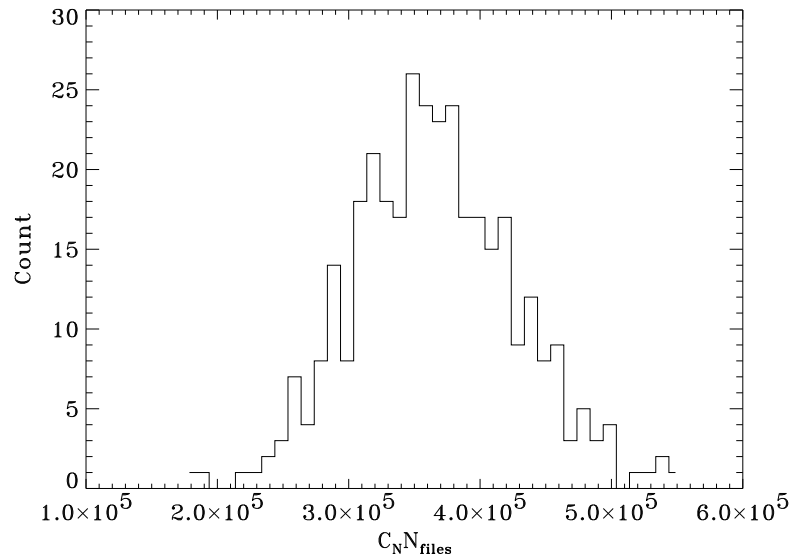


Figure 36 Histogram of  $C_N N_{\text{files}}$  for a stare lag of zero, modulation 5, channel 45.

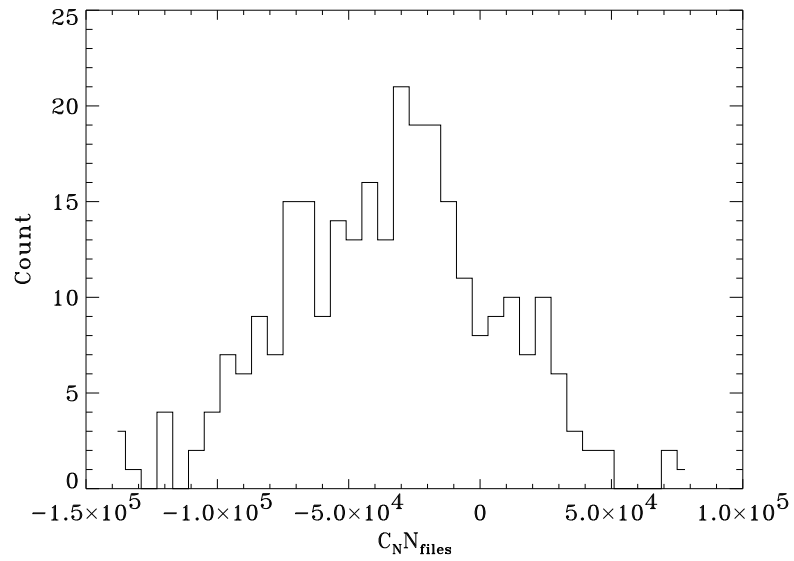


Figure 37 Histogram of  $C_N N_{\text{files}}$  for a stare lag of two, modulation 5, channel 45.

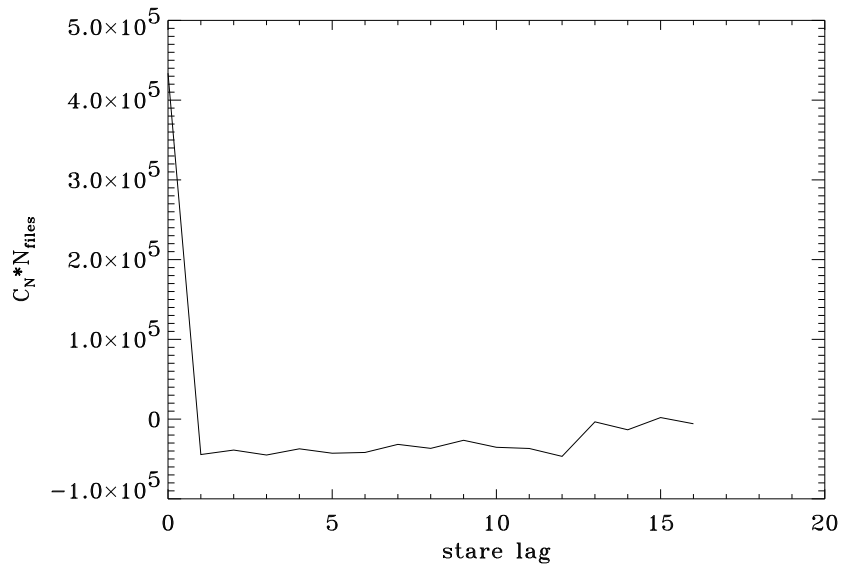


Figure 38  $C_N N_{\text{files}}$  vs. stare lag for modulation 5, channel 45 as an example.  $C_N N_{\text{files}}$  is not flat, but is tapered for non-zero lags.

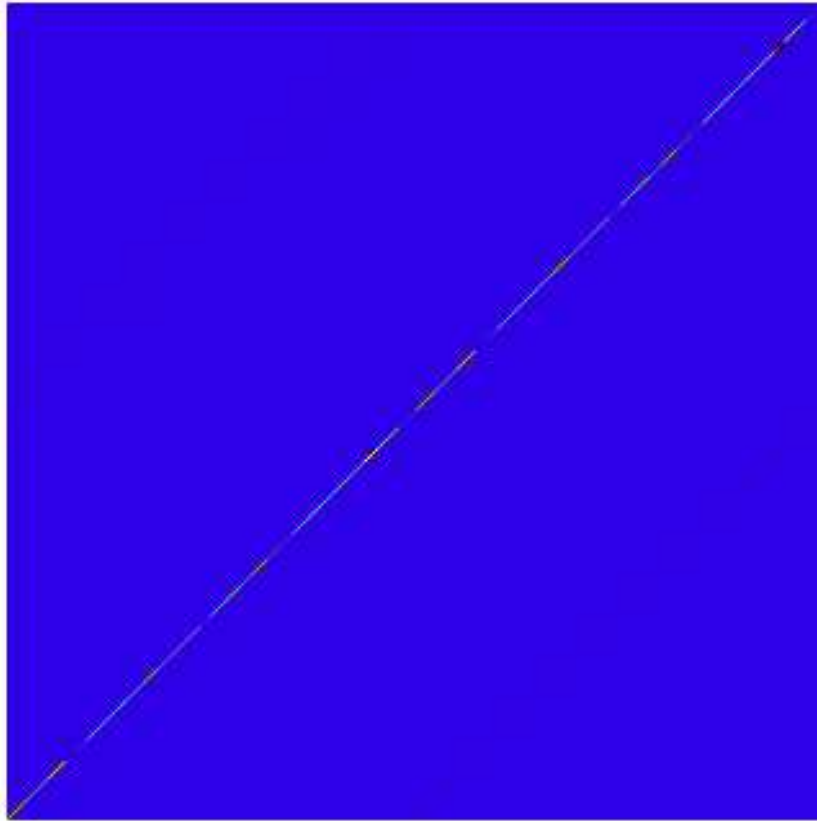


Figure 39 Noise covariance matrix,  $C^N$ , for modulation 2.  $C^N(1,1)$  is in the bottom left. The matrix is 690 x 690 for the 345 fields and 2 channels in the reduced, co-added data. Points 1:345 correspond to channel 45 and points 346:690 correspond to channel 12.

### 5.3 Internal Consistency Checks

Several self-consistency checks were performed on each modulation of the data set, using our best estimate of the noise covariance. We performed these same tests using the preliminary noise covariance, which suffers from sample variance, and found that the consistency tests failed. The tests indicate that the data set used is self consistent and that our best estimate of the noise

mode	$\chi^2$
1	615
2	660
3	603
4	600
5	667
6	710
7	640
8	609

Table 8  $\chi^2$  at best fit band power. Expected dof =  $690 - 31 \times 2 = 628$

covariance is indeed a good model for the noise.

### 5.3.1 $\chi^2$ Tests

The  $\chi^2 = \vec{d}^T \mathbf{C}^{-1} \vec{d}$ , where  $\vec{d}$  is the data vector and  $\mathbf{C} = \mathbf{C}^T + \mathbf{C}^N + \mathbf{C}^C$  is the total covariance, is consistent with its expected value (the number of degrees of freedom) in all modulations. Table 8 lists  $\chi^2$  for each modulation.

### 5.3.2 $\beta$ Tests

Since the two channels do not observe exactly the same points on the sky, a direct  $\chi^2$  test between them could not be done. Instead, the probability enhancement factor,  $\beta$ , (Knox et al. 1998) is computed between data from the two channels for each modulation.



The value of  $\beta$  is given by

$$\frac{1}{2}\ln|\mathbf{C}| + \frac{1}{2}\vec{d}^T \mathbf{C}^{-1} \vec{d} - \frac{1}{2}\ln|\mathbf{C}_{11}| - \frac{1}{2}\vec{d}_1^T \mathbf{C}_{11}^{-1} \vec{d}_1 - \frac{1}{2}\ln|\mathbf{C}_{22}| - \frac{1}{2}\vec{d}_2^T \mathbf{C}_{22}^{-1} \vec{d}_2 \quad (5.6)$$

where  $\mathbf{C}_{11}$  is the total covariance for the first channel,  $\mathbf{C}_{22}$  is the total covariance for the second channel, and  $\mathbf{C}$  is the total covariance for all of the pixels in each modulation. The expected value of  $\beta$  is given by

$$\langle \beta \rangle_0 = \frac{1}{2}\ln\left(\frac{|\mathbf{C}_{11}||\mathbf{C}_{22}|}{|\mathbf{C}|}\right) \quad (5.7)$$

and the variance of  $\beta$  is

$$\langle (\beta - \beta_0)^2 \rangle_0 = Tr(\mathbf{w}_{12}\mathbf{w}_{21}) \quad (5.8)$$

where

$$\mathbf{w}_{21} \equiv \mathbf{C}_{21}^T (\mathbf{C}_{11}^T + \mathbf{C}_{11}^N)^{-1} \quad (5.9)$$

and  $\mathbf{C}_{21}^T$  is the theoretical cross-covariance between the two channels.

The value of  $\beta$  falls within the expected range for all modulations when the best estimate noise matrix is used. This is not our strongest test because the signal-to-noise is weaker when each channel and modulation are considered separately.

### 5.3.3 *KL Decomposition*

Finally, the data set was transformed into the KL (signal-to-noise eigenmode) basis. In that basis,  $\mathbf{C}^{-1/2}\vec{d}$  should be Gaussian distributed with

$\sigma = 1$  and a total area equal to the number of degrees of freedom. Histograms of  $\mathbf{C}^{-1/2}\vec{d}$  are consistent with Gaussian distributions for all of the modulations for the best estimate noise matrices and are inconsistent with Gaussian distributions for the preliminary noise matrices. Figures 40 and 41 show histograms for one of the modulations using the best estimate noise matrix and preliminary noise matrix respectively.

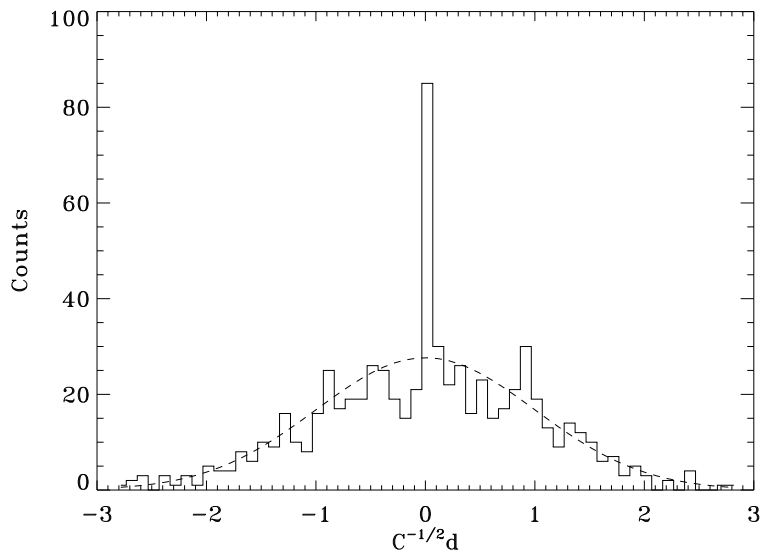


Figure 40 Distribution of  $\mathbf{C}^{-1/2}\vec{d}$  in the KL basis for modulation 7 using our best estimate noise matrix. The large spike at  $\mathbf{C}^{-1/2}\vec{d} = 0$  is due to modes which have been set to zero by the chopper constraint matrix. The histogram follows the expected Gaussian distribution.

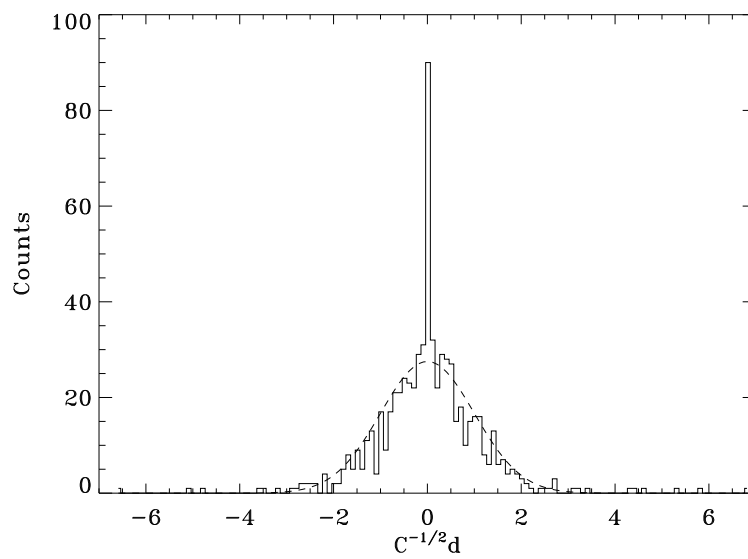


Figure 41 Distribution of  $\mathbf{C}^{-1/2}\vec{d}$  in the KL basis for modulation 7 using a preliminary noise matrix. The large spike at  $\mathbf{C}^{-1/2}\vec{d} = 0$  is due to modes which have been set to zero by the chopper constraint matrix. The number of counts in the central region are systematically lower than the number in the expected Gaussian distribution and there are many high  $\sigma$  points. This preliminary noise matrix also failed the  $\chi^2$  and  $\beta$  tests.

## CHAPTER 6

### CROSS-MODULATION ANALYSIS

An analysis including the cross-modulation correlations is presented in this chapter. This analysis is not simply a trivial expansion of the single modulation analysis presented in Chapter 5, but requires more sophisticated techniques for the estimation of the noise model and of the likelihood. Following the procedure of Wilson et al. (1999), the likelihood is simultaneously estimated in a series of 8 bands from a map which was constructed including all of the cross-modulation correlations. The results are consistent with those from the single modulation analysis. However, since this analysis includes the correlations between modulations, the constraints on the power spectrum can be used directly for cosmological parameter estimation.

#### 6.1 Noise Model and Consistency Checks

In order to derive a noise model for the cross-modulation analysis, we expanded the procedure of section 5.2 for the cross-modulation noise correlations. The value of  $\chi^2 = \vec{d}(\mathbf{C}^{\text{N}} + \mathbf{C}^{\text{C}})^{-1}\vec{d}^t$ , where  $\mathbf{C}^{\text{N}}$  includes noise correlations between all modulations, was computed for each observing set

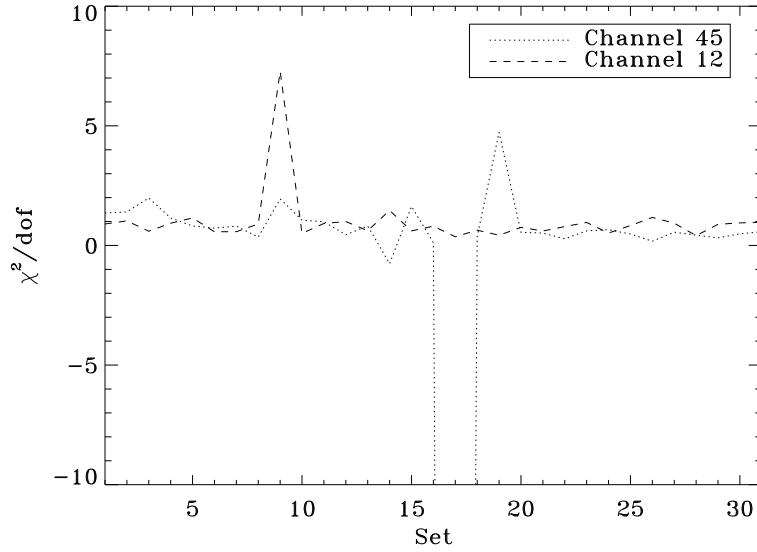


Figure 42  $\chi^2/\text{dof}$  for each set using an expansion of the noise model of section 5.2.  $\chi^2 = \vec{d}(\mathbf{C}^{\mathbf{N}} + \mathbf{C}^{\mathbf{C}})^{-1}\vec{d}^t$  and typical dof = 13 stars x 7 modulations - 7 constraints = 84. The  $\chi^2/\text{dof}$  are unacceptable, so a better model of the cross-modulation noise is necessary.

and channel. The results are shown in Figure 42 and indicate that a better model of the cross-modulation noise is necessary.

In general, the elements of the cross-modulation noise matrix can be expressed as

$$C_{ijmm'}^{\mathbf{N}} = C_{mm'}^{\mathbf{M}} C_{ij}^{\mathbf{F}}, \quad (6.1)$$

where the components of  $\mathbf{C}^{\mathbf{M}}$  are given by

$$C_{mm'}^{\mathbf{M}} = \vec{M}_m^t \mathbf{C}^{\mathbf{S}} \vec{M}_{m'} \quad (6.2)$$

and  $\vec{M}_m$  is the timestream modulation vector for modulation  $m$ ,  $\mathbf{C}^{\mathbf{S}}$  describes the noise in the timestream as a function of chopper sample  $s$  and  $\mathbf{C}^{\mathbf{F}}$  is a

model of the noise between fields  $i$  and  $j$ . Thus models for  $\mathbf{C}^{\mathbf{M}}$  and  $\mathbf{C}^{\mathbf{F}}$  are needed. For clarity,  $\mathbf{C}^{\mathbf{S}}$  is a  $128 \times 128$  matrix,  $\mathbf{C}^{\mathbf{M}}$  is a  $8 \times 8$  matrix, and  $\mathbf{C}^{\mathbf{F}}$  is a  $690 \times 690$  matrix for PyV.

In the single modulation analysis we effectively assumed  $\mathbf{C}^{\mathbf{S}}$  was the identity matrix. For white noise with the chopper offset removed,  $\mathbf{C}^{\mathbf{N}}$  would be of the form:

$$C_{ijmm'}^{\mathbf{N}} \propto \left(\delta_{ij} - \frac{1}{N_{\text{stares}}}\right) \sigma^2 \vec{M}_m^t \vec{M}_{m'} \quad (6.3)$$

However, a single  $\sigma$  does not characterize all modulations. Rather,  $\sigma$  decreases with increasing modulation, so a more sophisticated model for  $\mathbf{C}^{\mathbf{S}}$  is necessary.

Assuming  $\mathbf{C}^{\mathbf{S}}$  only depends on chopper sample separation  $\Delta s = s - s'$ , we can compute  $\mathbf{C}^{\mathbf{S}}$  from the following function:

$$f(\Delta s) = \sum_s d_s d_{s+\Delta s}. \quad (6.4)$$

For example, the  $C_{12}^{\mathbf{S}}$  component of  $\mathbf{C}^{\mathbf{S}}$  is given by  $f(\Delta s = 1)$ . In order to compute  $f(\Delta s)$ , a chopper synchronous offset is first subtracted from the raw data. Then  $f(\Delta s)$  is calculated for each channel, cycle and stare in a file.  $f(\Delta s)$  is then averaged over cycle, stare, and file. Figure 43 shows  $f(\Delta s)$  for each channel in one of the sets.

$\mathbf{C}^{\mathbf{M}}$  is calculated for each set and channel following equation 6.2.  $\mathbf{C}^{\mathbf{M}}$  matrices for channels 1 and 2 right and left are averaged, as are  $\mathbf{C}^{\mathbf{M}}$  matrices

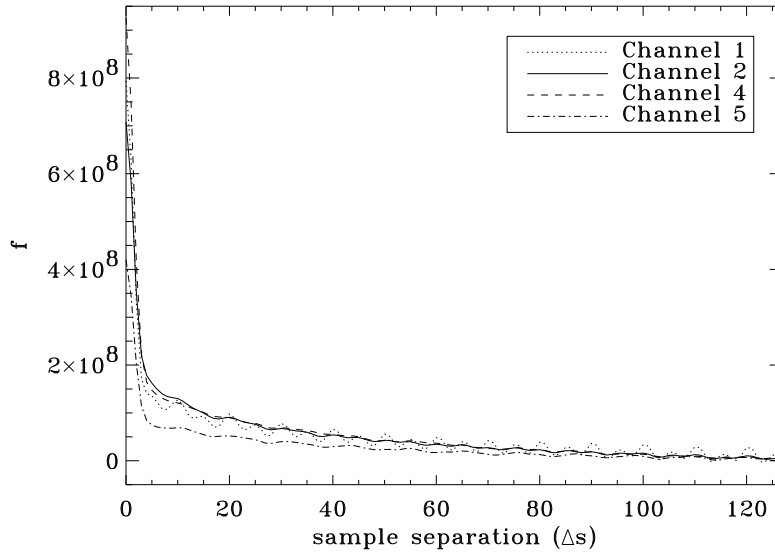


Figure 43  $f(\Delta s)$  for set hb9.  $f(\Delta s)$  breaks around  $\Delta s = 6$ , as would be expected from the beam size.

for channels 4 and 5 right and left, yielding  $\mathbf{C}^M$  matrices for channels 12 and 45 in each set. As an example,  $\mathbf{C}^M$  for one set and channel is shown in Figure 44.

In order to get a simple form for  $\mathbf{C}^F$ , we investigated the effect of ignoring the cross-channel correlations and the taper as a function of stare lag on the single modulation band powers. The results are shown in Figure 45. Ignoring the correlations between channels 12 and 45 and assuming the correlation between fields  $i$  and  $j$  come only from the chopper offset subtraction does not change the angular power spectrum significantly, so we assume  $\mathbf{C}^F$  is of that form for the cross-modulation analysis.

Finally, since this noise model is derived from sample-sample, it is larger

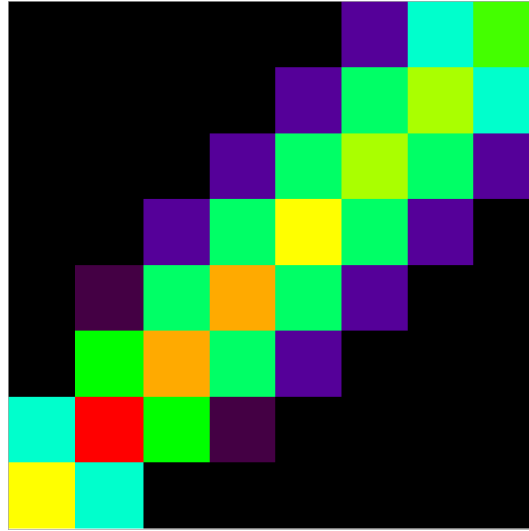


Figure 44  $\mathbf{C}^{\mathbf{M}}$  for set hb9, channel 45. Elements that are more than 2 modulations apart are relatively uncorrelated.

than the corresponding noise derived from the co-added data by a factor of  $\sim 10^4$ , so  $C_{ijmm'}^N$  must be normalized to the variance in the co-added data for each set. Since  $\mathbf{C}^{\mathbf{M}}$  accounts for the relative normalization of all of the modulations,  $C_{ijmm'}^N$  must be normalized to the variance in only one modulation of the co-added data for each set. We normalize to modulation 8 because it is least potentially affected by the ground shield. Figure 46 shows the  $\chi^2/\text{dof}$  for each set using the final cross-modulation noise model. If  $C_{ijmm'}^N$  is normalized to modulation 2 instead of modulation 8, the  $\chi^2$  depends on elevation (Figure 47).

As another check on the noise matrix used in the cross-modulation analysis, single modulation band powers were computed using the  $C_{ijmm}^N$  components of  $C_{ijmm'}^N$ . They are consistent with the band powers given in Chapter



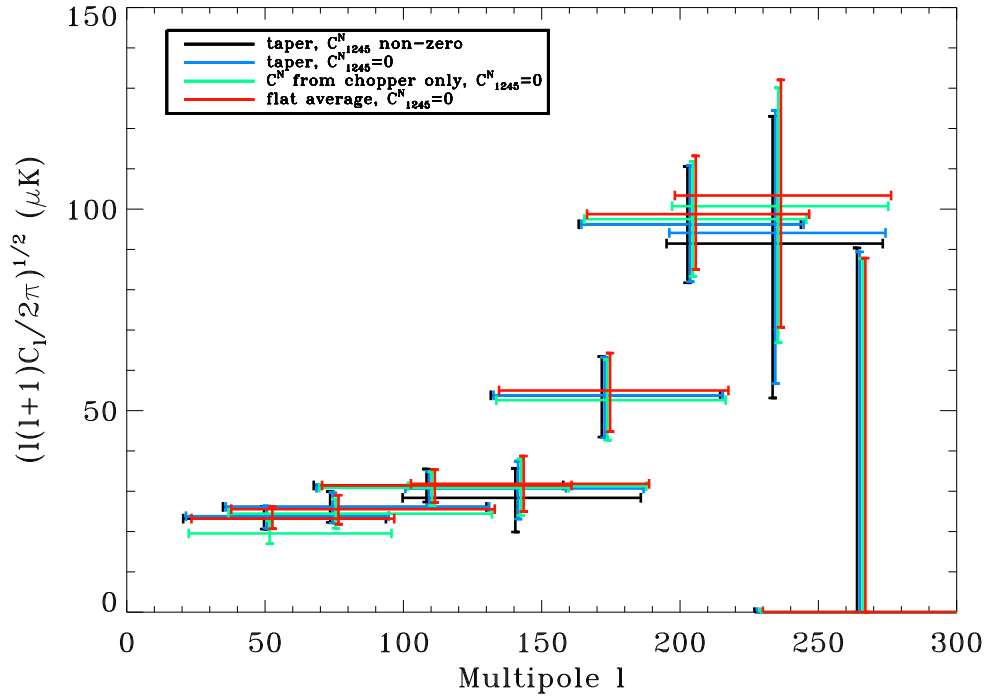


Figure 45 Angular power spectra obtained using 4 different noise models. Ignoring the correlations between channels 12 and 45 and the taper of  $C_N N_{files}$  as a function of stare lag does not change the angular power spectrum significantly.

5.

## 6.2 Map Making

The power spectrum is simultaneously estimated in several  $l$ -space bands, this time including all of the cross-modulation covariances, from a map constructed from the modulated data. The power spectrum could have been estimated using covariance matrices of size  $5520 \times 5520$  in each of the  $l$ -space

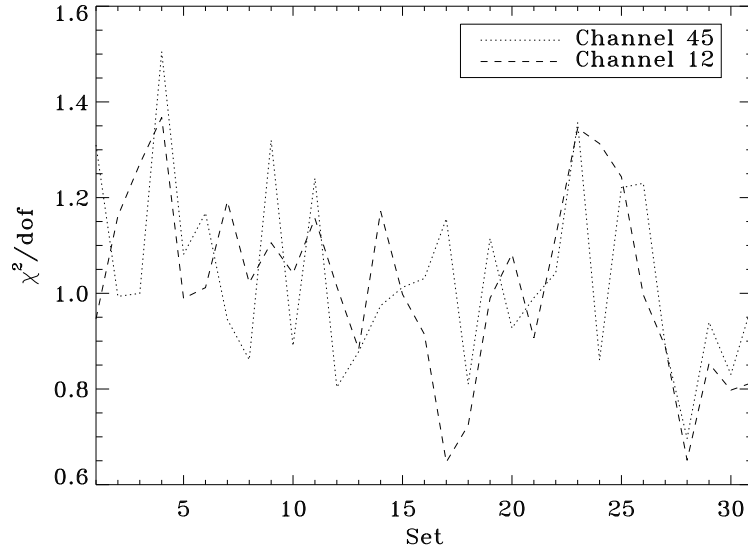


Figure 46  $\chi^2/\text{dof}$  for each set using the final noise matrix.  $\chi^2 = \vec{d}(\mathbf{C}^{\text{N}} + \mathbf{C}^{\text{C}})^{-1}\vec{d}^{\text{T}}$  and typical dof = 13 stars x 8 modulations - 8 constraints = 96. The vertical scale of the plot covers a smaller range than that of Figure 42.

bands, but transformation into a map basis first reduces the computational load. This technique was used in an analysis of the MSAM-I experiment (Wilson et al. 1999), for which the power spectrum estimated using the map is consistent with the power spectrum estimated directly from the full covariance matrices.

In order to construct the map, first recognize that the data can be expressed as

$$\vec{d} = \mathbf{B}\vec{T} + \vec{n} \quad (6.5)$$

with noise covariance matrix  $\langle nn \rangle = \mathbf{N}$ . (The actual  $\mathbf{N}$  used is  $\mathbf{N} = \mathbf{C}^{\text{N}} + \mathbf{C}^{\text{C}}$ .) To obtain the underlying temperature field  $\vec{T}$ , the matrix  $\mathbf{B}$

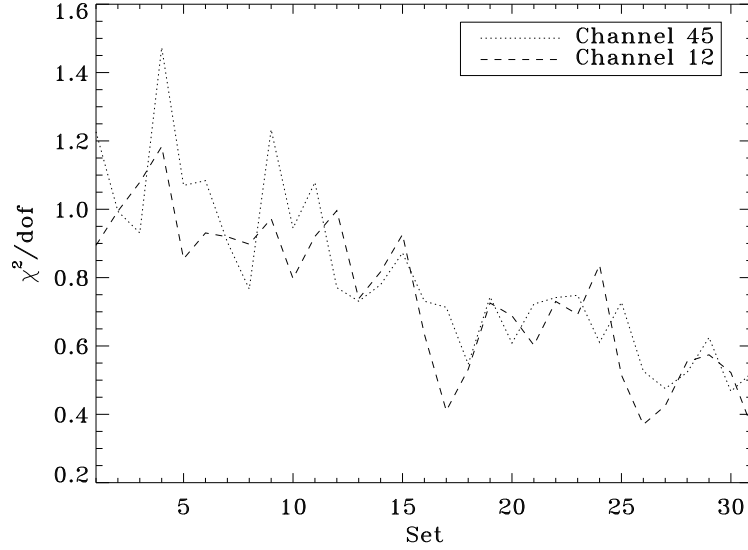


Figure 47  $\chi^2/\text{dof}$  for each set normalized to modulation 2.  $\chi^2 = \vec{d}(\mathbf{C}^{\text{N}} + \mathbf{C}^{\text{C}})^{-1}\vec{d}^{\text{t}}$  and typical dof = 13 stares x 8 modulations - 8 constraints = 96. The declination of the sets roughly decreases with increasing set number. The vertical scale of the plot covers a larger range than that of Figure 46.

must be inverted. This inversion is carried out by constructing the estimator

$\hat{T}$  which minimizes the  $\chi^2$ :

$$\chi^2 \equiv (\vec{d} - \mathbf{B}\hat{T})\mathbf{N}^{-1}(\vec{d} - \mathbf{B}\hat{T}). \quad (6.6)$$

We find

$$\hat{T} = \tilde{\mathbf{N}}\mathbf{B}\mathbf{N}^{-1}\vec{d}. \quad (6.7)$$

This estimator will be distributed around the true temperature due to noise,

where  $\tilde{\mathbf{N}}$ , the noise covariance matrix for the map, is given by

$$\tilde{\mathbf{N}} \equiv \langle (\hat{T} - \vec{T})(\hat{T} - \vec{T}) \rangle = (\mathbf{B}^{\text{T}}\mathbf{N}^{-1}\mathbf{B})^{-1}. \quad (6.8)$$

$l$	$(l(l+1)C_l/2\pi)^{1/2}$
$44_{-15}^{+15}$	$22_{-5}^{+4}$
$75_{-15}^{+15}$	$24_{-7}^{+6}$
$106_{-15}^{+15}$	$34_{-9}^{+7}$
$137_{-15}^{+15}$	$50_{-12}^{+9}$
$168_{-15}^{+15}$	$61_{-17}^{+13}$
$199_{-15}^{+15}$	$77_{-28}^{+20}$
$230_{-15}^{+15}$	$0.003_{-0.003}^{+87}$
$261_{-15}^{+15}$	$69_{-69}^{+71}$

Table 9 Angular power spectrum constraints from the cross-modulation analysis. Band powers are in  $\mu K$ .

### 6.2.1 Power Spectrum Constraints

This map can be analyzed in the same manner as the modulated data, with the advantage that the signal covariance matrix is much simpler to compute than using equations 4.3 and 4.21. In the map basis, the signal covariance matrix simplifies to

$$\langle T_i T_j \rangle = \sum_l \frac{2l+1}{4\pi} P_l(\cos(\theta_{ij})) C_l. \quad (6.9)$$

Indeed, one way to think of a map is that it is the linear combination of the data for which the signal (and therefore its covariance) is independent of the experiment. The noise covariance for the map (equation 6.8) accounts for all of the experimental processing.

The results of the likelihood analysis are shown in Figure 48 and are given in Table 9.

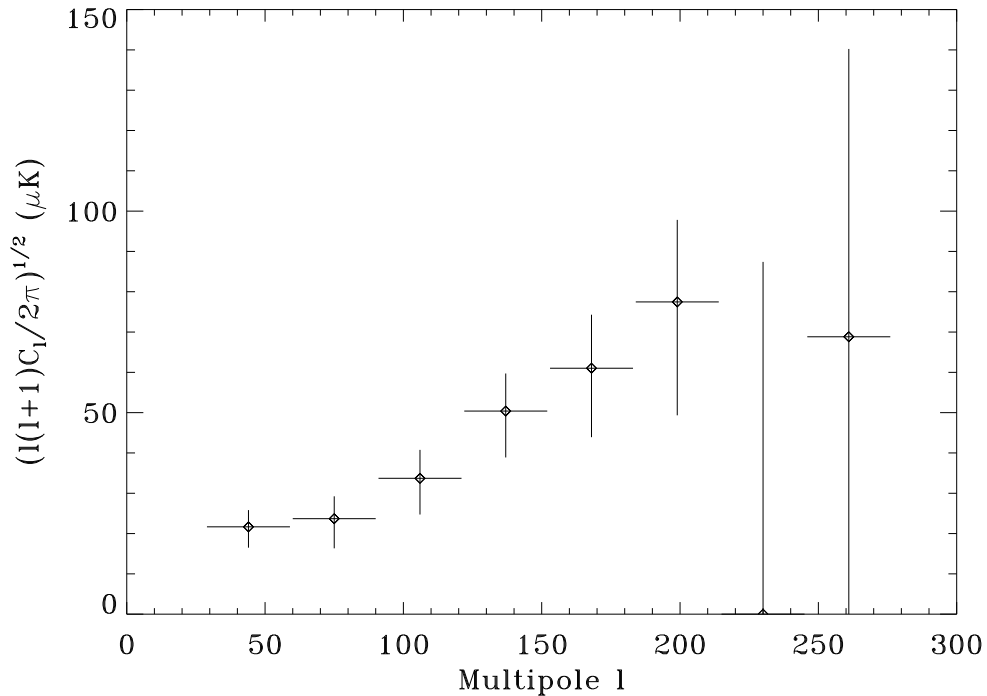


Figure 48 Angular power spectrum constraints from the cross-modulation analysis. Flat band power,  $(l(l+1)C_l/2\pi)^{1/2}$  is simultaneously estimated in 8  $l$ -space bands including cross-modulation theory and noise covariances. The error bars include statistical uncertainties only.

The angular power spectra obtained using the cross-modulation and single modulation analyses are consistent, as illustrated in Figure 49. At first glance, the band power in the fourth modulation of the single modulation analysis is higher than that of the fourth band of the cross-modulation analysis. However, the Knox minimum variance filter (Knox 1999) shows that the fourth modulation of the single modulation analysis has significant sensitivity to lower  $l$  scales. The Knox filter is a more complete representation of angular sensitivity than just the diagonal window functions, because it

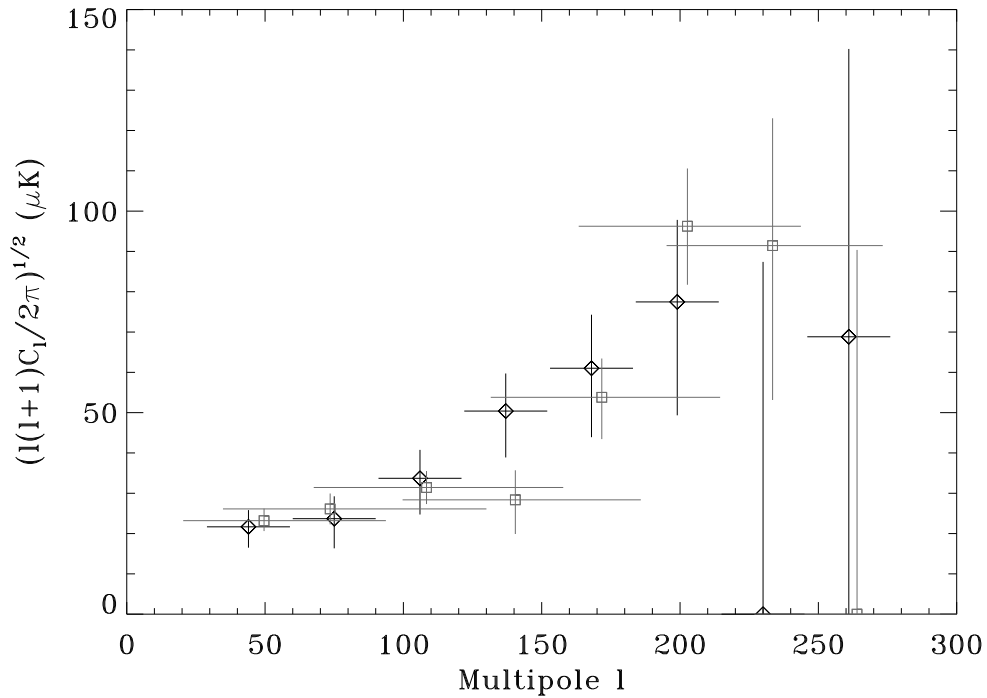


Figure 49 Comparison of angular power spectra from single and cross-modulation analyses. Points obtained from the single modulation analysis are denoted by gray squares and points obtained from the cross-modulation are denoted by black diamonds.

contains information from the full (off-diagonal) covariance matrix.

### 6.2.2 CMB Images

The map can also be Wiener-filtered to produce a realistic image of the sky. A Wiener-filtered map of the main PyV region and the  $S/N$  in the map are shown in Figure 50. The unfiltered map, not the Wiener-filtered map, was used for power spectrum estimation.

## 6.3 Comparisons With Other Experiments

### 6.3.1 Power Spectrum Comparison

Flat band powers calculated from the subset of PyV data in the PyIII region of sky are consistent with the PyIII flat band powers to within the uncertainties. Given the calibration and statistical uncertainties, the lowest  $l$  PyV modulation agrees with the the smallest scale COBE measurements.

### 6.3.2 Comparing PyV and PyIII Maps

Using the technique of section 6.2.1, maps of the sky are reconstructed from the PyIII data. The PyIII map is compared to the PyV map in the same region of the sky in Figure 51. Since PyIII has higher S/N than PyV, features which appear in the PyV map should also appear in the PyIII map, but features which appear in the PyIII map may not necessarily appear in the PyV map. In order to compare modes of the experiments which are similar to each other, both maps are transformed into the KL basis and only modes with  $S/N > 2$  are used. It is not necessary to Weiner filter the maps (which removes noise) if only the highest S/N modes are used. Structures found in the PyV map of Figure 51 are also evident in the PyIII map of Figure 51, implying that PyIII and PyV are consistent with each other.

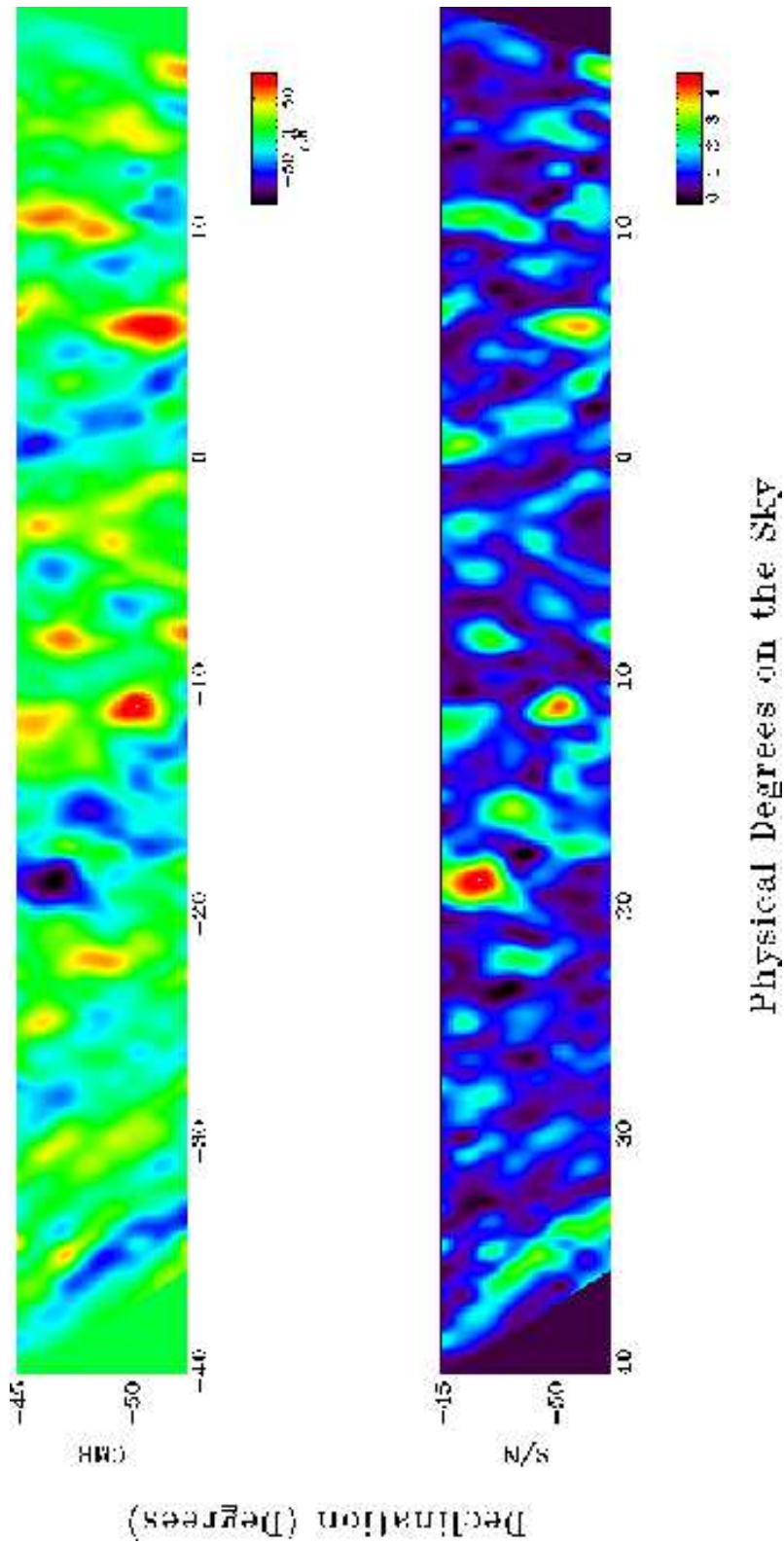


Figure 50 Wiener-filtered CMB and S/N maps for the main PyV region. The unfiltered map was used for power spectrum estimation.



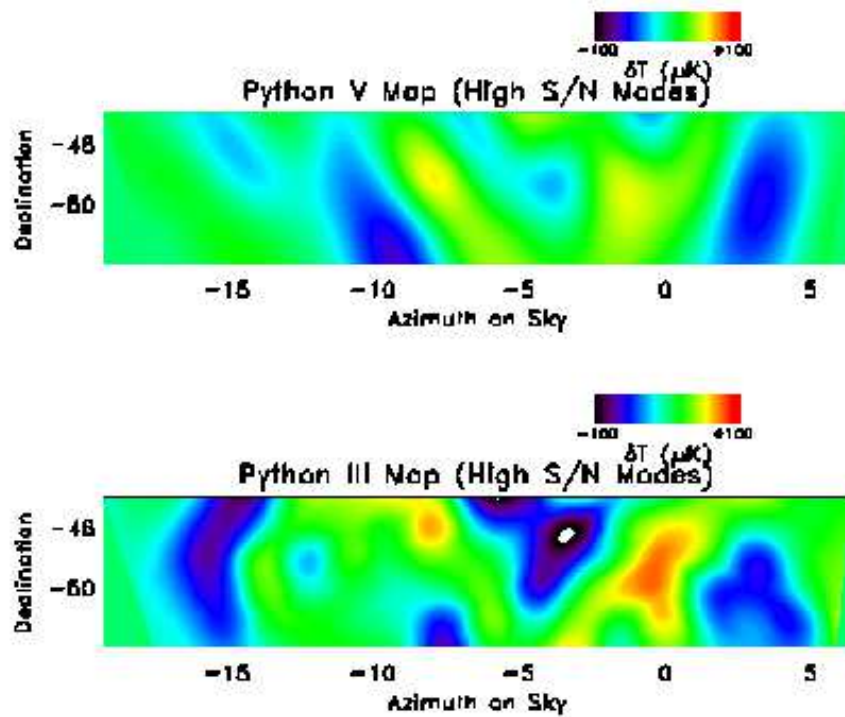


Figure 51 A comparison of PyV and PyIII maps. Structures found in the PyV map are also evident in the PyIII map, implying that PyIII and PyV are consistent with each other.

## CHAPTER 7

### FOREGROUNDS

The PyV data are cross-correlated with several foreground templates in order to set limits on possible foreground contamination. The templates used are the Schlegel et al. (1998) 100 micron dust map, which is based on IRAS and DIRBE maps, the Haslam et al. (1974) 408 MHz survey (synchrotron), and the PMN survey (point sources). Each foreground template map is smoothed to PyV resolution, pixelized and modulated according to the PyV observation scheme.

Two templates are created for the PMN survey. We call one PMN, which is converted to  $\delta T_{\text{CMB}}$  using the spectral indices given in the survey. The other we call PMN0, which is converted to a flux at 40 GHz assuming a flat spectrum extrapolated from the flux measurement at 4.85 GHz. The assumption of a flat spectrum is conservative in that it is likely to overestimate the flux at 40 GHz. Neither case is correct, since spectral indices have not been measured for all of the sources, in which case a flat spectrum is assumed, but we do know that some of them are not flat, so a flat spectrum will be inappropriate. The two cases cover a reasonable range of possibilities.

For each modulation and foreground template, a correlation coefficient

and uncertainty are calculated following de Oliveira-Costa et al. (1997):

$$\alpha = \frac{\vec{d}_f^t \mathbf{C}^{-1} \vec{d}_p}{\vec{d}_f^t \mathbf{C}^{-1} \vec{d}_f}; \sigma_\alpha^2 = \frac{1}{\vec{d}_f^t \mathbf{C}^{-1} \vec{d}_f} \quad (7.1)$$

where  $\vec{d}_f$  and  $\vec{d}_p$  are the modulated foreground and PyV data respectively and  $\mathbf{C} = \mathbf{C}^N + \mathbf{C}^C + \mathbf{C}^T$  (Figure 52).

A weighted mean and uncertainty over all of the modulations for each foreground are given in Table 10. In all cases there is no clear detection of foregrounds. The RMS of each modulation of each foreground was calculated and then multiplied by the corresponding  $1\sigma$  error bar in Table 10 in order to estimate an upper limit on the foreground contribution to CMB band power. The limits on contributions from foregrounds are given in Table 11 and are at least  $\sim 10\times$  smaller than the measured CMB bandpowers.

As a test on both the map-making procedure and the foreground estimation procedure, a map of the dust was constructed from the dust data which had been modulated and pixelized according to PyV observing strategy. The original dust map was recovered.

If the diffuse morphology of the sky is not constant as a function of wavelength, then these templates do not reveal all of the foreground contamination and more could be hidden in the PyV data. A combined analysis of PyIII at 90 GHz and PyV at 40 GHz would constrain the foreground contamination further.

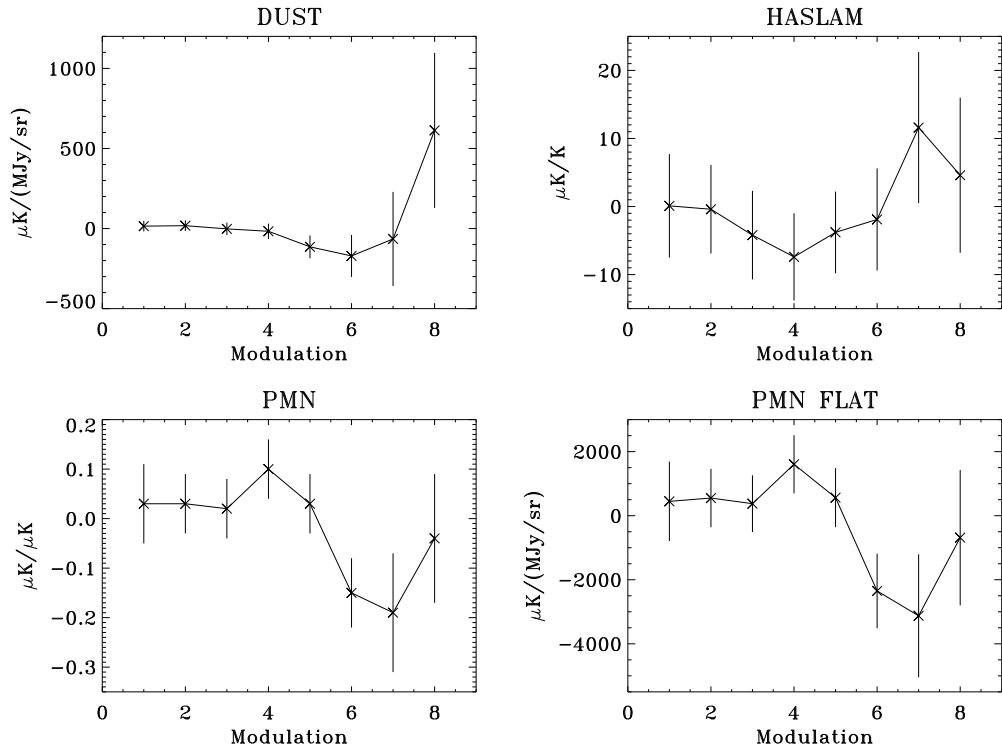


Figure 52 Correlation coefficients and uncertainties for each foreground and modulation.

Dust	Haslam	PMN	PMN0
$\mu K (MJy / sr)^{-1}$	$\mu K / K$	$\mu K / \mu K$	$\mu K (MJy / sr)^{-1}$
$-3 \pm 18$	$-2.0 \pm 2.6$	$0.012 \pm 0.024$	$195 \pm 385$

Table 10 Correlation coefficients and uncertainties for weighted means.

Mode	Dust	Haslam	PMN	PMN0
1	1.0	0.5	0.3	0.3
2	1.0	0.6	0.6	0.6
3	1.1	0.8	1.0	1.0
4	1.1	1.0	1.1	1.1
5	1.9	2.7	2.7	2.7
6	2.7	6.7	5.4	5.4
7	2.0	6.9	5.9	5.9
8	1.6	8.2	6.6	6.6

Table 11 Upper limits on foreground contribution. All units are  $\mu K$ .

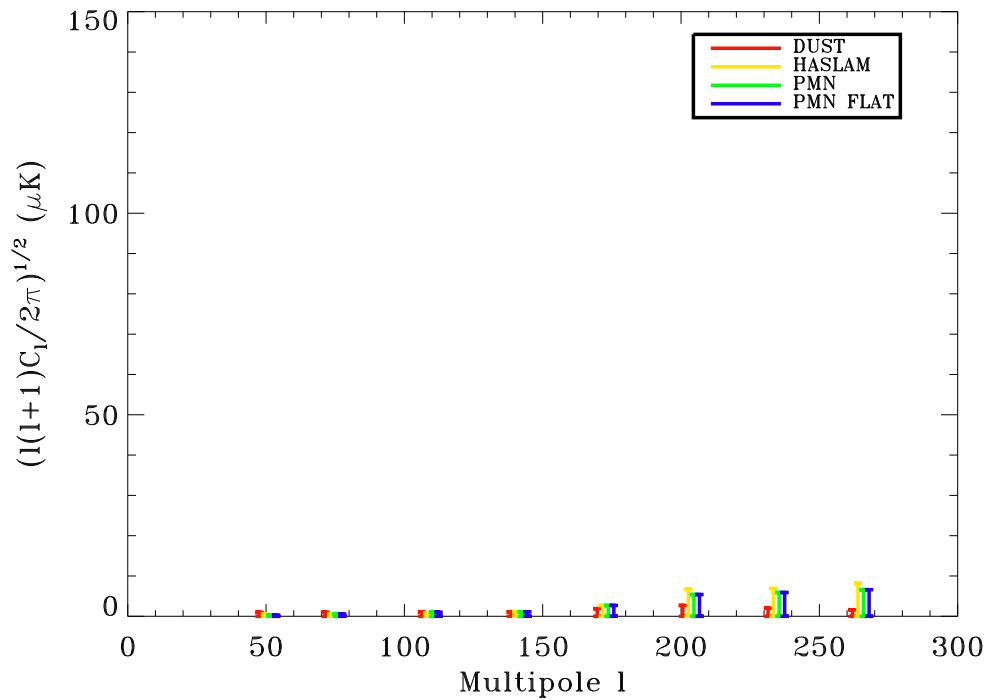


Figure 53 Upper limits on foreground contribution. All units are  $\mu K$ .

## CHAPTER 8

### CONCLUSIONS

The goal of the Python V season was to increase the sky coverage and the range of observed angular scales of the Python experiment thereby constraining the CMB angular power spectrum.

The PyV experiment fully samples 598 deg<sup>2</sup> of the microwave sky and constrains the CMB angular power spectrum in the angular scale range  $40 \lesssim l \lesssim 260$ . The measurements pass internal consistency checks, show little contamination from foreground radiation, and are consistent with previous Python and COBE results.

The results of experiments previous to PyV collectively imply a rise in the angular power spectrum, but the PyV experiment definitively shows a rise in the spectrum from from large ( $l \sim 40$ ) to small ( $l \sim 200$ ) angular scales. Figure 54 summarizes the constraints on the angular power spectrum by experiments previous to PyV and highlights the PyV results.

The PyV data are inconsistent with a flat spectrum, and instead show a rising spectrum, implying the acoustic scenario of structure formation described in the introduction is correct. The PyV data give confidence in results of estimation of cosmological parameters, such as  $\Omega$ , from all previous CMB

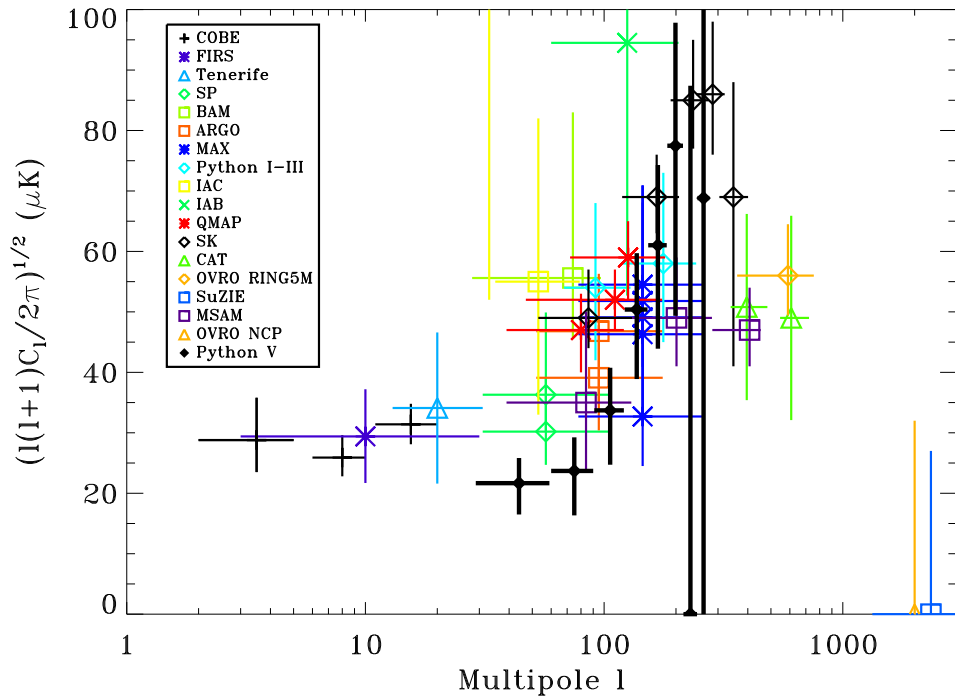


Figure 54 CMB anisotropy measurements as of Feb 1999. The points are the same as those in Figure 2. The PyV measurements are overlotted.

experiments because the rise in the spectrum could no longer be a calibration artifact. Since reionization of the universe would damp power at smaller angular scales (Hu and White 1995), the PyV data can rule out models of homogeneous reionization with  $z_{reion} \gtrsim 75$ . Earlier work on cosmic defect models suggests there would be no peak in the CMB angular power spectrum due to defects (Allen et al. 1997, Pen et al. 1998), in which case the PyV data would disfavor defect models. However, there is still disagreement in the predictions, with later work (Albrecht et al. 1999, Wu et al. 1998) suggesting there could be a peak due to defects. The PyV spectrum is shown in

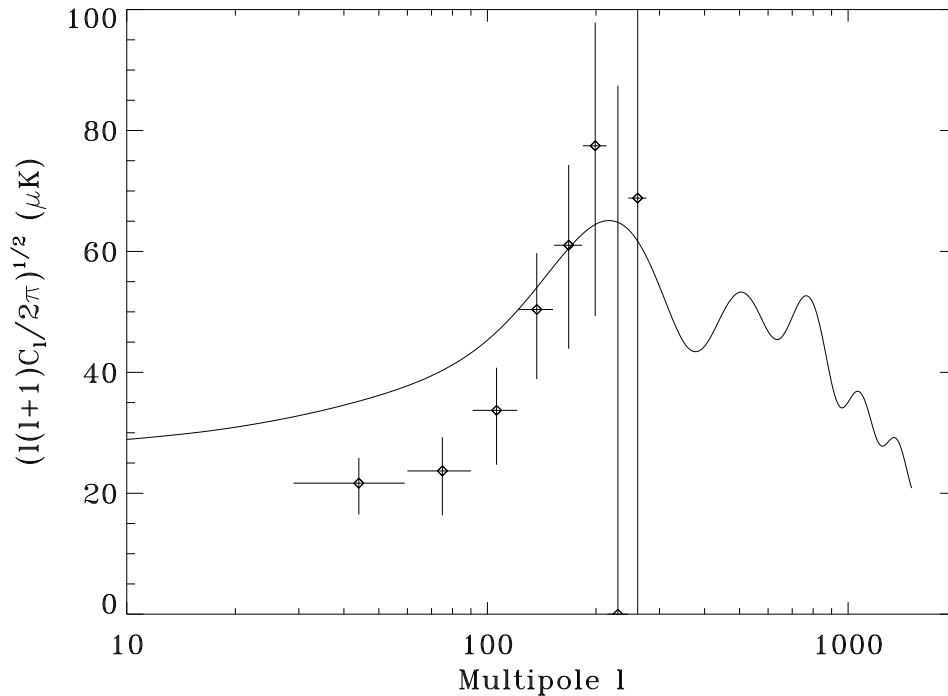


Figure 55 PyV angular power spectrum and COBE-normalized standard CDM model (density  $\Omega = 1.0$ , Hubble constant  $H_0 = 50$  km/s/Mpc, baryon density  $\Omega_b = 0.05$ , and cosmological constant  $\Lambda = 0.0$ ). Only statistical uncertainties are included in the PyV points.

reference to a COBE-normalized standard cold dark matter (sCDM) model in Figure 55. The PyV spectrum has lower power at large angular scales and a steeper slope than typical sCDM models ( $\chi^2/\text{dof} \sim 2.5$  for the model shown). Models with a higher baryon density and/or a cosmological constant have a steeper slope than the model shown. While future CMB experiments will estimate cosmological parameters to high precision in the coming decade, the robust rise in the Python V spectrum already tightly constricts the range of viable models of structure formation.



## REFERENCES

- Albrecht, A., Battye, R. A. and Robinson, J. 1999, Phys. Rev. D, 59, 023508
- Allen, B., Caldwell, R. R., Dodelson, S., Knox, L., Shellard, E. P. S. and Stebbins, A. 1997, Phys. Rev. Lett., 79, 2624
- Alvarez, D. 1996, Ph.d. thesis, Princeton Univ.
- J. R. Bond, [astro-ph/9407044](mailto:astro-ph/9407044)
- Bond, J. R., Jaffe, A., and Knox, L. 1998, Phys. Rev. D, 57, 2117
- BOOMERANG website, <http://www.physics.ucsb.edu/~boomerang>
- CBI website, <http://astro.caltech.edu/~tjp/CBI>
- Cheng, E. S., et al. 1997, ApJ, 488, L59
- Church, S. E. et al. 1997, ApJ, 484, 523
- Coble, K. et al. 1999, ApJ, 519, L5
- de Bernadis, P. et al. 1994, ApJ, 422, L33
- de Oliveira-Costa, A., Kogut, A., Devlin, M. J., Netterfield, C. B., Page, L. A., and Wollack, E. J. 1997, ApJ, 482, L17
- de Oliveira-Costa, A. et al. 1998, ApJ, 509, L77
- Devlin, M. J., de Oliveira-Costa, A., Herbig, T., Miller, A. D., Netterfield, C. B., Page, L. A., and Tegmark, M. 1998, ApJ, 509, L69
- Dicke, R. H., Peebles, P. J. E., Roll, P. G., and Wilkinson, D. T. 1965, ApJ, 142,414
- Dragovan, M., Ruhl, J. E., Novak, G., Platt, S. R., Crone, B., Pernic, R., and Peterson, J. B. 1994 ApJ, 427, L67 (PyI)
- Femenia, B., et al. 1998, ApJ, 498, 117
- Fixsen, D. J., Cheng, E. S., Gales, J. M., Mather, J. C., Shafer, R. A. and Wright, E. L. 1996, ApJ, 473, 576

- Gaier, T., Schuster, J., Gundersen, J., Koch, T., Seiffert, M., Meinhold, P., and Lubin, P. 1992, ApJ, 398, L1
- Ganga, K., Page, L., Cheng, E., and Meyer, S. 1994, ApJ, 432, L15
- Ganga, K., Ratra, B., Gundersen, J. O. and Sugiyama, N. 1996, astro-ph/9602141
- Griffin and Peterson 1998, private communication
- Gundersen, J. O., et al. 1995, ApJ, 443, L57
- Hancock, S. et al. 1997, MNRAS, 289,505
- Haslam, C.G.T., Salter, C.J., Stoffel, H. and Wilson, W.E. 1982, A&AS, 47, 1
- Herbig, T., de Oliveira-Costa, A., Devlin, M. J., Miller, A. D., Page, L. A., and Tegmark, M. 1998, ApJ, 509, L73
- Hinshaw, G., Banday, A. J., Bennett, C. L., Gorski, K. M., Kogut, A., Smoot, G. F., and Wright, E. L. 1996, ApJ, 464, L17
- Hu, W., Sugiyama, N., and Silk, J. 1997, Nature, 386, 37
- Hu, W. and White, M. 1995, astro-ph/9507060
- Kovac, J., Dragovan, M., Schleuning, D. A., Alvarez, D., Peterson, J. B., Miller, K., Platt, S. R., and Novak, G. 1999, in preparation (PyIV)
- Knox, L. 1999, astro-ph/9902046
- Knox, L., Bond, J. R., Jaffe, A., Segal, M., and Charbonneau, D. 1998, Phys. Rev. D, 58, 083004
- Leitch, E. M., Readhead, A. C. S., Pearson, T. J., Myers, S. T. and Gulkis, S. 1998, astro-ph/9807312
- Lim, M. A., et al. 1996, ApJ, 469, L69
- MAP website, <http://map.gsfc.nasa.gov>
- Masi, S., et al. 1996, ApJ, 463, L47
- Mather, J. C. et al. 1990, ApJ, 354, L37
- MATLAB User's Guide, The MathWorks, Natick, MA 1992

- Netterfield, C. B., Devlin, M. J., Jarosik, N., Page, L., Wollack, E. J. 1997, ApJ, 474, 47
- Pen, U., Turok, N. and Seljak, U. 1998, Phys. Rev. D, 58, 023506
- Penzias, A. A. and Wilson, R. W. 1965, ApJ, 142,419
- Peterson et al. 1998, private communication
- Picirillo, L. and Calisse, P. 1993, ApJ, 411, 529
- Planck website,  
<http://astro.estec.esa.nl/SA-general/Projects/PlanckSurveyor>
- Platt, S. R., Kovac, J., Dragovan, M., Peterson, J. B., and Ruhl, J. E. 1997, ApJ, 475, L1 (PyIII)
- Readhead, A. C. S. et al 1989, ApJ, 346,566
- Ruhl, J. E., Dragovan, M., Platt, S. R., Kovac, J., and Novak, G. 1995, ApJ, 453, L1 (PyII)
- Seljak and Zaldarriaga 1996, ApJ, 469, 437
- Schlegel, D. J., Finkbeiner, D. P. and Davis, M. 1998, ApJ, 500, 525
- Schuster, J., Gaier, T., Gundersen, J., Meinhold, P., Koch, T., Seiffert, M., Wuensche, C. A., and Lubin, P. 1993, ApJ, 412, L47
- Scott, P. F. et al. 1996, ApJ, 461, L1
- Smoot, G. F., et al. 1992, ApJ, 396, L1
- Tanaka, S. T. et al. 1996, ApJ, 468, L81
- Tegmark, M., Taylor, A. N. and Heavens, A. F., [astro-ph/9603021](http://astro-ph/9603021)
- TopHat website, <http://topweb.gsfc.nasa.gov>
- Torbet, E. et al. 1999, [astro-ph/9905100](http://astro-ph/9905100)
- Tucker, G. S. et al. 1996, [astro-ph/9611225](http://astro-ph/9611225)
- White, M, Carlstrom, J. E., Dragovan, M. and Holzappel, W. L. 1997, [astro-ph/9712195](http://astro-ph/9712195)
- White, M., Scott, D., and Silk, J. 1994,ARA&A, 32, 329

White, M. and Srednicki, M. 1995, ApJ, 443, 6

Wilson, G. W. et al. 1999 astro-ph/9902047

Wu, J. H. P., Avelino, P. P., Shellard, E. P. S. and Allen, B. 1998,  
astro-ph/9812156